Boundary-Layer Meteorology (2021) 178:249–281
https://doi.org/10.1007/s10546-020-00569-y

RESEARCH ARTICLE

Integration of a Building Energy Model in an Urban Climate Model and its Application

Luxi Jin[1] · Sebastian Schubert[1] · Daniel Fenner[2] · Fred Meier[2] · Christoph Schneider[1]

Received: 3 December 2019 / Accepted: 31 August 2020 / Published online: 20 September 2020

Abstract
We report the ability of an urban canopy model, coupled with a regional climate model, to simulate energy fluxes, the intra-urban variability of air temperature, urban-heat-island characteristics, indoor temperature variation, as well as anthropogenic heat emissions, in Berlin, Germany. A building energy model is implemented into the Double Canyon Effect Parametrization, which is coupled with the mesoscale climate model COSMO-CLM (COnsortium for Small-scale MOdelling in CLimate Mode) and takes into account heat generation within buildings and calculates the heat transfer between buildings and the urban atmosphere. The enhanced coupled urban model is applied in two simulations of 24-day duration for a winter and a summer period in 2018 in Berlin, using downscaled reanalysis data to a final grid spacing of 1 km. Model results are evaluated with observations of radiative and turbulent energy fluxes, 2-m air temperature, and indoor air temperature. The evaluation indicates that the improved model reproduces the diurnal characteristics of the observed turbulent heat fluxes, and considerably improves the simulated 2-m air temperature and urban heat island in winter, compared with the simulation without the building energy model. Our set-up also estimates the spatio–temporal variation of wintertime energy consumption due to heating with canyon geometry. The potential to save energy due to the urban heat island only becomes evident when comparing a suburban site with an urban site after applying the same grid-cell values for building and street widths. In summer, the model realistically reproduces the indoor air temperature and its temporal variation.

Keywords Building energy model · Citizen weather station · COSMO-CLM · Indoor temperature · Urban heat island

✉ Luxi Jin
luxi.jin@geo.hu-berlin.de

[1] Geography Department, Humboldt-Universität zu Berlin, Unter den Linden 6, 10099 Berlin, Germany

[2] Chair of Climatology, Institute of Ecology, Technische Universität Berlin, Rothenburgstraße 12, 12165 Berlin, Germany

1 Introduction

Within cities, near-surface air temperatures are typically higher than in their rural surroundings. This is known as the urban-heat-island (UHI) effect, and the temperature difference between the urban and the rural areas is then referred to as UHI intensity. In mid-latitude cities, UHI intensities are especially pronounced during night-time and in summer (Yagüe et al. 1991; Fortuniak et al. 2006; Erell and Williamson 2007; Fenner et al. 2014; Skarbit et al. 2017). Among other factors, urban near-surface air temperatures are increased by heat storage and its subsequent release, and anthropogenic heat emissions (Oke 1982), which are associated with the emissions from buildings, human metabolism, industry and power plants, and vehicle exhaust. Among all sources, the heat release from urban buildings is considered the largest contributor to anthropogenic sensible and latent heat emissions (Sailor 2011; Chrysoulakis and Grimmond 2016). The seasonal variation of anthropogenic heat emissions depends on the climate and the demand for cooling or heating (Sailor 2011; Chow et al. 2014). In winter, in regions where heating is required, anthropogenic heat fluxes influence screen-level temperatures in urban areas extensively due to the dominant heat emission and the shallower boundary layer (Bohnenstengel et al. 2014). A temperature increase of up to 1.5 K due to anthropogenic heating was observed in central London, U.K., on a calm and cloud-free day in December (Bohnenstengel et al. 2014). Fan and Sailor (2005) detected an increase of the UHI intensity of 2 K to 3 K during a winter night in Philadelphia, U.S.A. In summer, waste heat originating from air conditioning systems affects air temperatures in urban areas in low/mid-latitude (Ohashi et al. 2007; Chow et al. 2014; Salamanca et al. 2015; Takane et al. 2017).

Sailor (2011) listed three methods for estimating anthropogenic heat, including inventory approaches, an energy budget closure, and building energy models (BEM). He recommended the latter for the building sector, as the BEM approach calculates the energy consumption within buildings and heat rejection explicitly, and considers both sensible and latent heat emissions. Different treatments of urban anthropogenic heat fluxes using the BEM approach have been investigated in recent years. The Town Energy Budget model (TEB, Masson 2000) calculates heat fluxes from buildings by dynamically solving the energy processes in buildings while assuming a constant inner building temperature, and has been extensively evaluated and applied in many studies (e.g., Lemonsu et al. 2004, 2015; Pigeon et al. 2008). Trusilova et al. (2013) applied the TEB model to the mesoscale climate model COSMO-CLM (COnsortium for Small-scale MOdelling in CLimate Mode, hereafter named CCLM) to extend the surface-layer parametrization, suggesting that it is important to use an urban parametrization on fine spatial resolutions (0.025°); the coupled CCLM–TEB approach better replicates the magnitude of the UHI intensity in Berlin, Germany, than the uncoupled one.

EnergyPlus (Crawley et al. 2001), an industry-standard building energy simulation program with detailed definition of specific air conditioning, applies an energy balance to compute the energy demand of buildings and the waste heat emissions from air conditioning. EnergyPlus is able to capture the real performance of air conditioning, including the loss of efficiency, a more realistic moisture exchange, and to take building-demand-reduction strategies into account. A coupling of EnergyPlus and the TEB model by Bueno et al. (2011) showed that this coupled system is capable of predicting energy consumption in Toulouse, France.

One of the first attempts to explicitly calculate the heat exchange of the building interior and exterior was presented by Kikegawa et al. (2003), who coupled their parametrization to different models to evaluate energy demand, the UHI effect, and health impacts (e.g., Kikegawa

et al. 2014; Ohashi et al. 2014; Takane et al. 2015, 2017). Similarly, a BEM approach was developed by Salamanca et al. (2010) (hereafter called the original BEM approach) and coupled with a multi-layer urban canopy model (Salamanca and Martilli 2010). The original BEM approach includes the heat generation within buildings, and the heat exchange between buildings and the atmosphere. When coupled with a mesoscale model, a feedback system between the indoor energy consumption and outdoor air temperature is established (Salamanca and Martilli 2010). Various applications for different cities verified the ability of this approach to reproduce temperatures and flow properties (Salamanca et al. 2011, 2012), and the citywide diurnal cycle of electricity consumption due to air conditioning (Salamanca et al. 2013, 2014, 2015). Another approach to incorporate anthropogenic heat into climate models is to prescribe the surface anthropogenic heat flux at the lowest layer of the atmosphere (Flanner 2009; Wouters et al. 2015, 2016).

Here, we present a new approach that couples the Double Canyon Effect Parametrization (DCEP, Schubert et al. 2012) with an integrated BEM approach into the mesoscale climate model CCLM (Rockel et al. 2008b). The DCEP scheme is a multi-layer urban canopy parametrization based on the Building Effect Parametrization (BEP, Martilli et al. 2002) for calculating the energy, radiation, and momentum fluxes from roof, wall, and ground surfaces within an urban street canyon. Compared with the original BEP scheme, the DCEP scheme conserves the total incoming radiation energy and accounts for neighbouring street canyons. The coupling of the DCEP scheme with the CCLM has been shown to be able to simulate typical characteristics of the urban boundary layer (Schubert and Grossman-Clarke 2014). However, the DCEP scheme only calculates the interactions within a street canyon without consideration of the building interior, which inaccurately depict UHI characteristics in winter (Trusilova et al. 2016). The new coupled DCEP–BEM scheme extends the original by adding an indoor environment with heating and cooling facilities into multi-storey buildings, and by incorporating a more comprehensive treatment of radiation through windows. Additionally, we present a considerable simplification of the radiative part, with only negligible effects on model results. This coupled model follows the concept of the original BEM approach and adjusts the room configuration and radiation routine explicitly.

Here, we evaluate the DCEP–BEM scheme within the CCLM extensively with respect to energy fluxes and near-surface air temperatures for a cold winter period and an extreme hot and dry summer period in 2018 for several measurement sites in and around Berlin. Based on the simulations, we explore the impact of anthropogenic heat emissions from the building interior onto the exterior in the urban area of Berlin, the response of indoor temperature to outdoor temperature during the summer period, and the spatio–temporal variation of simulated energy consumption due to anthropogenic heat including heating systems in the winter period.

Below, Sect. 2 presents a detailed description of the coupled urban–mesoscale model, with the simulation set-up, description of the research area, and the observations for evaluation given in Sects. 3–5. Results are presented and discussed in Sect. 6, with a summary and conclusions given in Sect. 7.

2 Model Description

The CCLM is a three-dimensional, fully compressible, and non-hydrostatic limited-area regional climate model (Rockel et al. 2008b), able to simulate time spans of up to centuries, and spatial resolutions between 1 and 50 km. It is an extension of the COSMO-Model operated

by the German Meteorological Service (DWD) and is developed by several weather services and organizations.

In order to allow for a realistic representation of cities, CCLM was coupled with the DCEP scheme (Schubert et al. 2012), which is a multi-layer urban canopy parametrization based on the BEP scheme (Martilli et al. 2002). Together, these parametrizations compute the momentum and sensible heat fluxes as well as the radiation budget of roof, wall, and ground surfaces based on the incoming radiation and meteorological variables (e.g., air temperature, atmospheric humidity, air pressure, air density, and velocity) from a mesoscale climate model. Both parametrizations describe the urban surface with quasi two-dimensional street canyons comprising a ground surface, a row of buildings, and two walls. The DCEP scheme adds a neighbouring canyon to include roofs in the radiation exchange, and DCEP differentiates between diffuse and direct shortwave radiation.

The original BEM approach by Salamanca et al. (2010) considers the anthropogenic heat of buildings by accounting for the heat generation within buildings and calculates the heat exchange between buildings and the atmosphere. The BEM approach treats buildings as hollow rather than solid structures because air and building material have different thermal properties. Moreover, the indoor temperature evolution is computed as a function of energy generation and consumption within the buildings, the radiation transmitted through the windows, the heat diffusion through the building structures, and the air conditioning.

Four sources determine indoor sensible heat loads. The first source is the radiation in a room, including the shortwave and longwave radiation that propagates from outdoors to indoors through windows and is reflected by interior surfaces. The second is the heat diffusion through building materials. The third is the anthropogenic heating generated by occupants (i.e., from human activity) and equipment (i.e., electrical devices) within a room. The fourth is ventilation, which relies on temperature differences to promote heat exchange between indoor and outdoor environments. Indoor latent heat loads are altered by occupants, ventilation, and air conditioning, but not conduction, because the urban surfaces within the DCEP framework are assumed to be completely impervious.

Below, we present our enhanced DCEP and BEM versions and the coupling with the CCLM.

2.1 Enhancements of the Urban Scheme

Quasi-two-dimensional street canyons are characterized by their building width B, street width W, and canyon length D (Fig. 1). Since the canyon length D is supposed to have a negligible effect on results, its value is chosen rather arbitrarily, but selected to be much

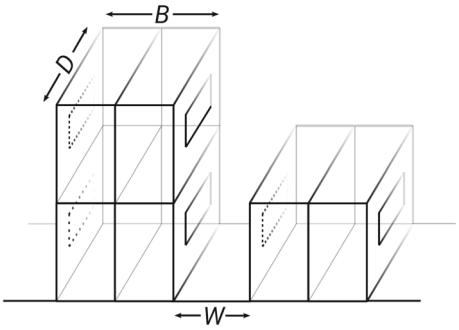

Fig. 1 Morphology of a quasi-two-dimensional street canyon showing buildings and a street, with B, W, D representing the building width, the street width, and the canyon length, respectively. Note that for the latest DCEP version, we implement the limit $D \to \infty$

larger than the values of B and W. Taking the limit $D \to \infty$ simplifies the formulation of the radiative part of the model considerably, without practically changing the results. The detailed mathematical formulations are listed in Appendix 1. The remaining aspects of the parametrization are left unchanged and the reader is referred to Schubert et al. (2012) for further details.

2.2 Coupling of the Urban and the Building Energy Model with the Mesoscale Model

2.2.1 Room Concept

The original BEM approach by Salamanca et al. (2010) is based on room elements embedded in buildings, with each room element consisting of a floor, a roof (ceiling), and four external walls with one window each. In the real case, though, a room often contains one window (or one window set) and this window is usually positioned in the wall facing the street. Therefore, rooms facing different orientations receive contrasting solar energy, which results in a temperature difference even on the same floor (Walikewitz et al. 2015).

In order to capture this variability due to room orientation, we implement two sub-rooms separated by an internal wall on each level of the building (Fig. 1). For each room, there is a window on the external wall facing the street. This two-room concept considers the variation in incoming radiation.

For consistency with the DCEP scheme, the limit $D \to \infty$ is introduced when coupling the BEM approach with the DCEP scheme, which eliminates consideration for the front and back side of a building. Thus, each room has two vertical surfaces (the internal and external wall) and two horizontal surfaces (the floor and ceiling).

2.2.2 Shortwave Radiation Received by Indoor Surfaces

In the original BEM approach, shortwave radiation penetrates through windows and redistributes uniformly onto the interior surfaces to be captured and reflected by wall surfaces. Hence, the total amount of the shortwave radiation received by an indoor surface i is $Rs_i = Rs + \sum_{j \neq i} \alpha_j Rs_j \psi_{ji}$ (identical to Eq. 13 in Salamanca et al. 2010). Here, Rs_i is the sum of the shortwave radiation directly captured by the indoor surface Rs, and the shortwave radiation reflected by the other indoor surfaces $\sum_{j \neq i} \alpha_j Rs_{\mathrm{wall},j} \psi_{ji}$, where α_j represents the albedo of the surface j, ψ_{ji} denotes the view factor from surface j to surface i, and Rs_j indicates the shortwave radiation reaching an indoor surface j.

Since in the DCEP–BEM approach a window is only located on an external wall, the interior surface of the external wall (surface 2) does not receive any shortwave radiation. Hence, we differentiate the calculation of shortwave radiation R_s between different surfaces (cf. Eq. 1). Here, $i, j = 1, 2, 3, 4$ represent the internal wall, the external wall, the floor, and the ceiling, respectively. The first term Rs is no longer the same at all surfaces as in the original BEM approach, but is a function of the view factor from the external wall (surface 2) to the surface i (Eq. 2). More information on the view factors is given in Schubert et al. (2012). The term Rs_{wind} refers to the incoming shortwave radiation through windows. The second term $\sum_{j \neq i} \alpha_j Rs_{\mathrm{wall},j} \psi_{ji}$ describes the radiation reflected by the other indoor surfaces, and remains the same as in the original BEM approach

$$Rs_i = \begin{cases} Rs + \sum_{j \neq i} \alpha_j Rs_j \psi_{ji} & \text{for } i = 1, 3, 4,\ j = 1, 2, 3, 4 \\ \sum_{j \neq i} \alpha_j Rs_{\mathrm{wall,j}} \psi_{ji} & \text{for } i = 2,\ j = 1, 2, 3, 4 \end{cases}, \tag{1}$$

with

$$Rs = Rs_{\text{wind}}\psi_{2i} \qquad \text{for } i = 1, 3, 4\,. \tag{2}$$

In this sense, the DCEP–BEM coupling enhances the physical consistency of the indoor energy balance regarding shortwave radiation.

2.2.3 Anthropogenic Heat Flux

Similar to the original BEM approach, the effect of air conditioning is also implemented in our coupled model, where air conditioning refers to heating in winter and cooling in summer. When in use, the indoor temperature and humidity can be controlled, which enables the estimation of the energy consumption for heating and cooling by the model.

In winter, the energy consumption for heating can be considered as the anthropogenic heat flux generated by the heating of the indoor environment, and transported outdoors through wall conduction or natural ventilation. In summer during cooling, an extra heat flux is produced and injected into the atmosphere as waste heat consisting of the heat to be removed from indoors and the energy consumption required for cooling. The calculation of waste heat follows the original BEM approach (Salamanca and Martilli 2010). In the DCEP–BEM coupling, two types of air conditioning for the rejection of waste heat are considered. One is located on the vertical walls with each floor having its own outdoor unit, which emits waste heat vertically into the atmosphere. The other is located on the rooftop of each building, controlling the indoor environment for the whole building and releasing its total waste heat into the atmosphere. The effects of different air conditioning are not evaluated in this study because indoor cooling is not widely used in Berlin (Umweltbundesamt 2013).

2.3 Coupling of the Urban and the Building Energy Model with the Mesoscale Model

The DCEP and coupled DCEP–BEM schemes require input data for the target urban area characteristics (e.g., the fraction of the natural and urban surface, the building-height distribution, the building and street width). With the help of the urban properties, the momentum fluxes, surface energy, and radiation from the mesoscale model are averaged for each grid cell, separated by natural and urban areas.

The BEM indoor environment is coupled with the DCEP walls and windows. The sensible heat flux acts between the inside and outside through DCEP walls, while latent heat exchange occurs through windows. Waste sensible and latent heat released from the air conditioning installed on the exterior walls can alter air temperature and the humidity in DCEP canyons. The temperature and humidity at the urban scale along with other calculated urban tendency terms are then interpolated back into the mesoscale height levels and included in the calculation of temperature, turbulence kinetic energy, and wind speed (Schubert et al. 2012).

3 Simulation Set-up

In order to evaluate the performance of the coupled model system for the urban area of Berlin, we conduct simulations for a winter period from 15 February 2018 0000 UTC to 10 March 2018 2300 UTC, and a summer period from 25 July 2018 0000 UTC to 17 August 2018 2300 UTC, with the first five days disregarded as spin-up for each simulation. The

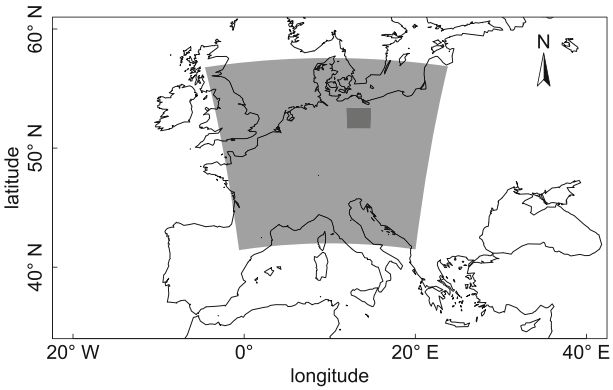

Fig. 2 Nested domains of a two-step dynamical downscaling driven by ERA5 reanalysis data with a spatial resolution of 31 km. The outer domain (central Europe) and the inner study area (Berlin, Germany) have a grid spacing of 7 km and 1 km, respectively

simulations are compared with reference runs consisting of only the existing DCEP approach. The COSMO5.0-CLM9 version is used for a two-step one-way nesting, i.e., horizontal grid spacing of 7 km (without urban scheme) and 1 km (with the urban scheme, with and without the BEM approach) (Fig. 2). The 7-km simulation is centred in the middle of Germany and covers central Europe with a domain size of 250 × 250 grid points. The 1-km simulation covers the area of Berlin with 195 × 195 grid points.

The CCLM runs use a two-time-level third-order Runge–Kutta split-explicit scheme (Wicker and Skamarock 2002) for time integration with timesteps of 40 s and 10 s for the 7-km and 1-km runs, respectively. The planetary-boundary-layer scheme is based on Mellor and Yamada (1982) and Raschendorfer et al. (2003). The radiation scheme by Ritter and Geleyn (1992) is applied for the radiative transfer. The lateral boundary conditions are derived from one-way nesting by a Davies-type lateral boundary formulation (Davies 1976). A multi-layer soil model with a vegetation parametrization is employed for both resolutions. Convection is handled by the Tiedtke (1989) parametrization for the 7-km set-up, and by a shallow-convection parametrization, which is a reduced Tiedtke approach for the 1-km set-up. The formation of grid-scale clouds and precipitation is parameterized by a microphysics scheme based on Kessler (1969). In addition to the basic Kessler-type scheme, 7-km runs involve cloud ice in representing precipitation formation in water, mixed phase, and ice clouds; the 1-km runs additionally include the graupel phase to the hydrological cycle (Doms et al. 2018).

The initial and lateral boundary conditions for the coarser 7-km run are provided by the global reanalysis dataset ERA5 (Copernicus Climate Change Service 2017). Spectral nudging (Rockel et al. 2008a) is used for both nesting steps. External parameters (i.e., the orography, monthly vegetation, and soil parameters) are created by the EXTPAR software system (External Parameter for Numerical Weather Prediction and Climate Application WebPEP[1], Smiatek et al. 2008) for the CCLM preprocessor. This climatologically constant field provides vegetation parameters and roughness lengths for the coarser simulations representing the complete grid cell. Within the DCEP component, these parameters should only represent the vegetated part in a grid cell. Therefore, for the 1-km runs, the data from the surroundings of Berlin are adopted for the urban area of Berlin for the winter and summer simulations. Leaf area

[1] https://www.clm-community.eu/.

Table 1 Building parameters of the urban surfaces

	Roof	Wall	Ground
Emissivity	0.90	0.90	0 .95
Thermal diffusivity ($m\,s^{-2}$)	0.67×10^{-6}	0.67×10^{-6} innermost layer: 0.01×10^{-6}	0.29×10^{-6}
Heat capacity ($J\,m^{-3}\,K^{-1}$)	1.769×10^{6}	2.250×10^{6}	1.940×10^{6}
Albedo	0.163	0.162	0.162

The values follow Martilli et al. (2002), Roessner et al. (2011), Schubert and Grossman-Clarke (2013)

indexes of $1.1\,m^2\,m^{-2}$ and $3.5\,m^2\,m^{-2}$; plant cover fractions of 0.48 and 0.88; root depths of 1.5 m and roughness lengths of 0.02 m and 0.13 m are used for this purpose.

The coupled urban DCEP–BEM approach is applied to the 1-km simulation. The urban structure and canopy parameters, which are derived in Schubert and Grossman-Clarke (2013) are based on a dataset with over 460,000 three-dimensional buildings in the City Geography Markup Language level of detail 2 format (CityGML LOD2). In this format, buildings are modelled with polygons representing ground, wall and roof surfaces. We use four street directions ($-45°, 0°, 45°, 90°$ from north) with spatially resolved urban structure and canopy parameters for each direction.

We adjust the building parameters for Berlin explicitly. The thicknesses of the external wall, the internal wall, the roof of a building, and the ground of a street canyon are 0.315 m, 0.2 m, 0.1575 m, and 0.5375 m, respectively. Further building parameters of urban surfaces are listed in Table 1. The area fraction of windows in the external wall is set to 0.2. The temperatures of the urban surfaces for all simulations are initialized with 273 K and 296 K for winter and summer, respectively. For the winter simulation, the indoor temperature is regulated based on indoor temperature measurements (Fig. 4) which are described in Sect. 5, to incorporate heating-system information. In addition, the air infiltration due to natural ventilation is set to 0.1 for the day (0700–1800 UTC) and zero for the night (1900–0600 UTC), considering that dwellers may open the window and vent a room regularly during the day. For the summer simulation, the air infiltration is set to 0.25 during all hours of a day. In contrast to the winter simulation, the indoor temperature during the summer period is not fixed and is to be modelled since only about 1–2% of the residential buildings are equipped with air conditioning in Germany (Umweltbundesamt 2013).

In Berlin, the average living space is 39.6 m^2 per habitant (Bureau of Statistics Berlin-Brandenburg 2019), which we convert to 0.025 person m^{-2} in the model. Additionally, metabolic sensible and latent heat production, and sensible heat generation due to equipment (except for heating or cooling devices), are set to 160 W per person, 22.7 W per person, and $7.4\,W\,m^{-2}$, respectively (cf. Salamanca and Martilli 2010).

4 Study Area and Period

Berlin is located in north-eastern Germany, between 52.3°N and 52.7°N and 13°E and 13.8°E, has a population of around 3.7 million people (2018), and 70.5% of its area is covered by human settlement (including buildings and streets) (Statistisches Bundesamt 2018). Berlin has flat terrain with numerous lakes and rivers, and the climate is characterized by temperate oceanic climate (Köppen-Geiger: Cfb, Kottek et al. 2006).

This study focuses on 2018, Germany's warmest and driest year since the beginning of regular temperature measurements in 1881 (Friedrich and Kaspar 2019). Compared to the average from 1981 to 2010, the annually-averaged air temperature at the Berlin-Alexanderplatz site operated by DWD was +2.2°C. Positive temperature anomalies occurred throughout the year except for March. Compared to the average of 1981–2010, the mean air temperature in March was 2.7°C lower in 2018 (Fig. 13 in Appendix 2), while the mean air temperature of July and August increased by 2.6°C and 3.3°C, respectively. The year 2018 had an annual precipitation amount of 477 mm, which is 114 mm (20%) less than the average for the period 1981–2010. The largest negative precipitation anomaly occurred in August with −93%.

For the winter period, the daily temperature remained below 0°C, and the lowest temperature dropped to −11.8°C on 2 March 2018 at the Berlin-Alexanderplatz site. Short showers occurred during the night of 15 February 2018 and in the morning of 5 March 2018. A rain event with a total amount of 8 mm lasted from late afternoon of 6 March 2018 to noon of 7 March 2018. Scattered rain fell on 8 March 2018 and reached a maximum rate of 3 mm h^{-1} around midnight. On 10 March 2018, the Berlin-Alexanderplatz site again measured some precipitation. The total precipitation of the investigation period at Berlin-Alexanderplatz is 16 mm.

The summer period was dominated by high pressure over north-west Europe, leading to a heatwave consisting of 16 hot days[2]. The constant sunny weather was interrupted at around midnight of 4 August 2018 when a convective cell moved along the southern fringe of Berlin and brought some precipitation. In the course of this event, parts of Berlin were covered by cumulus and stratocumulus clouds during 5 August 2018. The precipitation amount at Berlin-Alexanderplatz during the whole summer period is 3 mm.

5 Measurements and Data for Model Evaluation

5.1 Turbulent Heat Fluxes

Turbulent heat fluxes for evaluating model simulations are derived from the measurement data at the energy-balance site Charlottenburg (cf. Table 2 and Fig. 3) operated by the Technical University of Berlin (TUB). The measurement system is installed on top of a 10-m tower above the roof of a 46-m high building. Average heights of buildings and vegetation for a 500-m radius around the side are 18 m and 11 m, respectively. Land cover is dominated by impervious surfaces (40%) and buildings (28%). The Charlottenburg site is surrounded by a canal (Landwehrkanal) on the northern and north-eastern side and a large green area (Tiergarten, about 2.1 km^2) on the eastern and south-eastern side.

Turbulent sensible Q_H and latent Q_E heat fluxes are derived from an eddy-covariance system, which combines an open-path gas analyzer and a three-dimensional sonic anemometer-thermometer (IRGASON, Campbell Scientific, Logan, Utah, USA) for simultaneous measurements of carbon dioxide and water-vapour density as well as orthogonal velocity components. The software package EddyPro (Version 6.2.1) is used to quality control the raw data (see Appendix 4 for details) and to calculate Q_H and Q_E values from 20-Hz time series over 30-min intervals, and then further averaged to hourly mean values. Details of the measurements and processing of radiative flux data are presented in Appendices 3 and 4.

[2] A "hot day" is defined as a day with a maximum temperature equal or higher than 30°C. This criterion is widely used in Germany and Austria.

Table 2 Data availability for measurements sites used for the evaluation of model simulations; Local Climate Zone: Stewart and Oke (2012); a.s.l. is above sea level

Station name	Network	Coordinates	Altitude a.s.l. (m)	Measurements	Class	Local Climate Zone	Site description
Alexanderplatz	DWD	52.52°N 13.41°E	36	2-m air temperature	Urban	5	Built-up area in the city centre surrounded by small scattered vegetation
Buch	DWD	52.63°N 13.50°E	60	2-m air temperature	Suburb	6	Sparsely built-up area with low population density
Kaniswall	DWD	52.40°N 13.73°E	33	2-m air temperature	Rural	B	Large open area with grass field; ≈ 30 km south-east from Alexanderplatz
Kigaramler	TUB	52.55°N 13.40°E	48	2-m air temperature Indoor air temperature	Urban	5	Built-up area with building blocks; a green park in the west; a railway station in the north
Lindenberg	DWD	52.21°N 14.12°E	98	2-m air temperature	Rural	9	Vegetated area; ≈ 65 km south-east from Alexanderplatz
Rothenburg	TUB	52.46°N 13.32°E	47	2-m air temperature indoor air temperature	Urban	6	Sparsely built-up area with large amounts of vegetation; botanical garden in the south-west
Charlottenburg	TUB	52.51°N 13.33°E	46	Turbulent heat fluxes	Urban	5	Built-up area with sparse vegetation; a park with large amounts of vegetation in the east

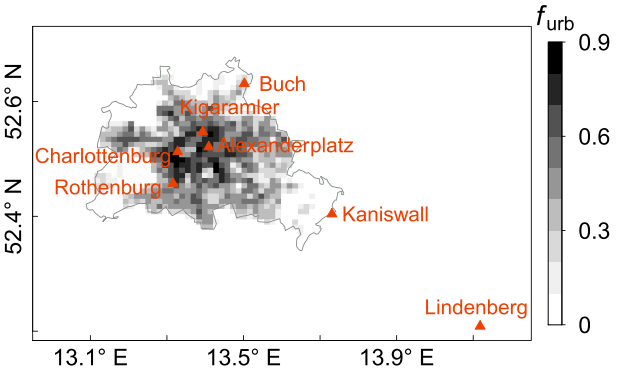

Fig. 3 Urban fraction (f_{urb}) of the city area of Berlin. Triangles indicate the observational sites, the city border of Berlin is depicted with the grey line

5.2 The 2-m Air Temperature

Air temperature at 2-m height at the DWD meteorological sites is measured with a LTS2000T probe (Eigenbrodt, Knigsmoor, Germany) in white radiation shields with an accuracy of ±0.2 K (Kaspar et al. 2013). Air temperature of the Urban Climate Observation Network of the TUB (Fenner et al. 2014) is measured by Campbell Scientific CS215 probes (specified accuracy for air temperature ±0.4 K in the range 5–40°C), installed in white radiation shields and actively ventilated during sunlit periods. Data from these sites have previously been used for the validation of mesoscale models (Kuik et al. 2016; Jänicke et al. 2017). Raw measurement data at 1-min resolution are quality controlled as described in Meier et al. (2017) with additional checks for persistence (same value for ≥ 2 h) and spikes (5 K threshold from one measurement to the next). For consistency with the DWD measurements, the 1-min average value at 10 min before each full hour is used for validation.

5.3 Indoor Temperature

For the derivation of the diurnal-heating cycles during the winter period (Fig. 4) and the evaluation of the indoor air temperature during the summer period, data from citizen weather stations (CWS) of the Netatmo company (www.netatmo.com) are used. Data of this type of station have previously been used for analyses of outdoor atmospheric conditions in Berlin (Fenner et al. 2017, 2019; Meier et al. 2017; Napoly et al. 2018). The accuracy of the sensors itself is within the specified accuracy range of ±0.3 K (Meier et al. 2017). Netatmo stations (Netatmo, Boulogne Billancourt, France) consist of two modules, one measuring indoor, the other outdoor atmospheric conditions. Outdoor data can be obtained freely via the company's application-programming interface. A full description of the stations and data collection can be found in Meier et al. (2017).

Two types of CWS data are used here and are described as follows:

1. *Indoor air temperature at known indoor locations*
   Citizen weather stations at two locations are operated by the TUB, with one at the Rothenburg site located in an office room on the first floor of a two-story building. The room is oriented towards the south and the sensor is located on the north side of the room. The other CWS at the Kigaramler site is situated in a playroom of a kindergarten, located

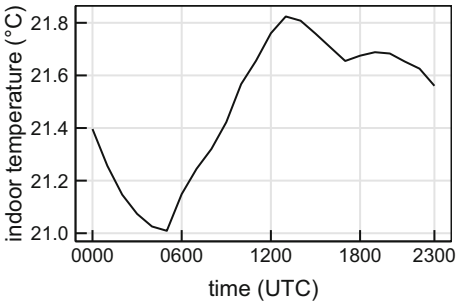

Fig. 4 Averaged diurnal cycle of observed indoor temperature at 30 CWS sites during the winter period

on the first floor of a four-story building in a room oriented to the south. Directly adjacent to the room is a large sunlit terrace. Raw data at 5-min resolution from both sites were aggregated to hourly mean values. Data from these two sites are used for evaluation of indoor temperature, and combined with data from five additional known indoor CWS locations and 23 deduced locations (see below) to derive an average diurnal-heating cycle during the winter period.

2. *Air temperature from deduced indoor locations*
As noted by Meier et al. (2017), crowdsourced CWS data of outdoor air temperature can actually contain indoor data if the owners use their outdoor devices to monitor indoor conditions. While these data are undesired for analyses of outdoor conditions, they are potentially useful for indoor applications. Therefore, we identify these sites by adapting a filter mechanism developed by Meier et al. (2017). We use crowdsourced CWS outdoor air-temperature data for Berlin as described in Meier et al. (2017) and deduced likely indoor stations from this dataset. For this, we first calculate the daily median value per CWS for the winter period if $\geq$ 80% of hourly values per day are available. Second, we calculate the mean $\overline{\chi}$ and standard deviation σ of the daily aggregated values for the entire winter period, omitting stations with $<$ 80% data availability. Third, possible indoor locations are determined if 18°C $< \overline{\chi} <$ 30°C and $\sigma <$ 2°C. Finally, data at these locations are visually checked by the authors to confirm that they are plausible indoor time series of air temperature. Finally, we obtain an averaged indoor temperature from 23 deduced indoor CWS, combined with data at seven known locations, for the winter period (Fig. 4).

5.4 Energy Consumption for Heating in February and March

Since there is no specific database related to the observed daily energy consumption for Berlin, we use a rough estimate of this value for comparison with our model results. In Berlin, 34% of the households use gas, 33% use oil, 29% use district heating, 2% use coal, and 3% use domestic night storage heating as a heating source (Berlin, Senate Department for Urban Development and Housing 2010). According to Schlomann et al. (2004), the annual consumption in Germany of gas, oil, district heating, domestic storage heating, and coal in Germany is about 162 kW h m^{-2}, 197 kW h m^{-2}, 111 kW h m^{-2}, 65 kW h m^{-2}, and 123 kW h m^{-2}, respectively. This results in an approximate annual consumed energy for heating per building plan area of 157 kW h m^{-2} in Berlin. Assuming that 13% and 12.5% of this amount are used in February and March, respectively (Stadtwerk 2019), we obtain a daily consumed energy of 0.73 kW h m^{-2} and 0.63 kW h m^{-2} for February and March, respectively.

6 Results

The simulation performance is evaluated using the mean bias error (MBE)

$$m = \frac{1}{n}\sum_{i=1}^{n}(P_i - O_i), \tag{3}$$

where P and O are the predicted and observed values, respectively, and n is the number of samples, and the root-mean-square error (r.m.s.e.)

$$r = \sqrt{\frac{1}{n}\sum_{i=1}^{n}(P_i - O_i)^2}. \tag{4}$$

6.1 Surface Energy Balance at the Charlottenburg Site

The observed surface turbulent fluxes depend on fetch areas, which are related to the wind speed and direction, as well as surface structures such as buildings and trees (Heilman et al. 1989). To investigate the surface area that contains a large percentage of the observed flux and its connection with the measurement height, fetch-to-height ratios (i.e., the fetch divided by the sensor height), are discussed in many studies (Panofsky and Townsend 1964; Rosenberg et al. 1984), with values ranging from 10:1 to 200:1. Based on a cumulative turbulent flux footprint analysis for the Charlottenburg site (not shown), we include model values of the corresponding grid cell as well as an adjacent grid cell in each direction. Figure 5 shows the diurnal cycles of surface turbulent sensible Q_H and latent Q_E heat fluxes, with shaded areas denoting the range of fluxes within the fetch. Note that while the model-derived fluxes Q_H and Q_E refer to the respective fluxes at the surface, the observed ones denote the fluxes received by the instrument situated above the roof of a building (Sect. 5.1). A positive value of the model-derived Q_H or Q_E indicates the flux from the surface emitting to the atmosphere; a negative value implies the flux directed towards the surface.

The observed Charlottenburg heat flux Q_H (bold points in Fig. 5a,b) has a clear daily variation, remaining almost constant through the night, before rising during the morning transition. The observed value of Q_H reaches a maximum at 1200 UTC (126 $\mathrm{W\,m^{-2}}$ in winter and 247 $\mathrm{W\,m^{-2}}$ in summer) and then decreases until sunset. In winter, the DCEP-derived Q_H (red shaded area surrounded by dotted lines in Fig. 5a) shows a diurnal pattern similar to the observed, however, with a considerable underestimation, in particular during night-time by at least 21 $\mathrm{W\,m^{-2}}$. The DCEP–BEM derived Q_H (red shaded area surrounded by solid lines in Fig. 5a) is substantially increased compared with that simulated with the DCEP approach alone. This is caused by the additional heat loads of the building interior associated with indoor heating systems, equipment, and occupants in the DCEP–BEM approach. The DCEP–BEM simulated heat fluxes are found with the range of the measurements, indicating both an enhancement compared with the DCEP approach and the feasibility of the above-mentioned fetch method. In contrast to the winter case, heating is not required in summer. Consequently, only a small increase of the surface sensible heat flux resulting from indoor occupants, equipment, and the natural ventilation is produced by the DCEP–BEM simulation (Fig. 5b). In summer, the observed Q_H values fall within the range of the modelled Q_H for both the DCEP and the DCEP–BEM approaches.

The observed surface latent heat flux Q_E in winter is $< 13\,\mathrm{W\,m^{-2}}$ (Fig. 5c) due to little precipitation and little transpiration of plants (cf. Sect. 4). During the summer period, the

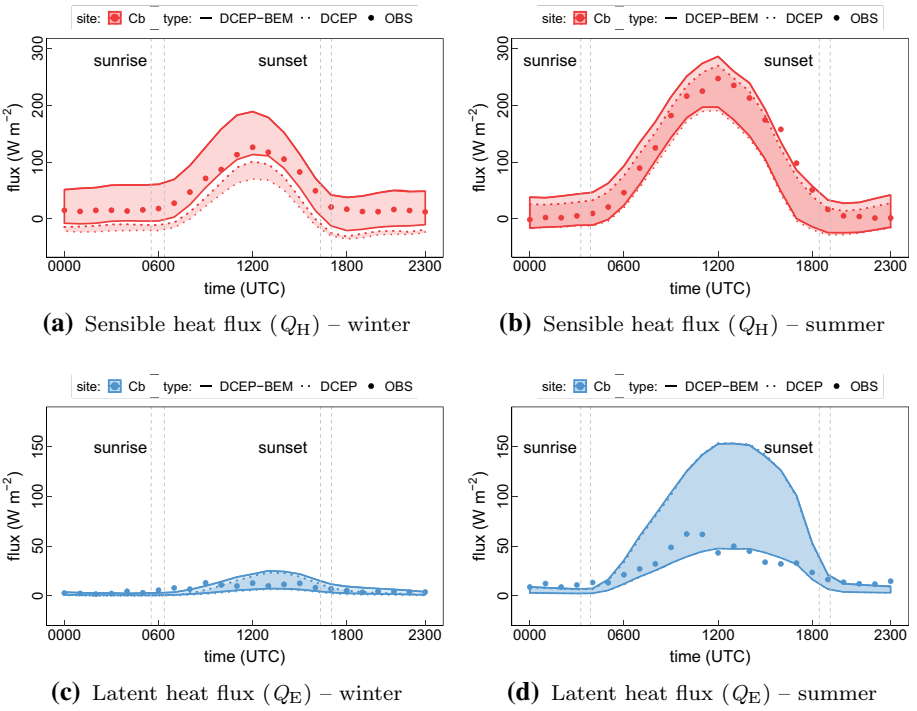

(a) Sensible heat flux (Q_H) – winter

(b) Sensible heat flux (Q_H) – summer

(c) Latent heat flux (Q_E) – winter

(d) Latent heat flux (Q_E) – summer

Fig. 5 Averaged diurnal cycle of surface fluxes (Q_H and Q_E) at the Charlottenburg (Cb) site for the simulation periods. The panels **a**, **c** denote the winter period (15 February 2018 0000 UTC to 10 March 2018 2300 UTC) and the panels **b**, **d** denote summer period (25 July 2018 0000 UTC to 17 August 2018 2300 UTC). Bold points refer to measurements (OBS). Dotted and solid lines refer to the DCEP and DCEP–BEM simulations, respectively. Vertical grey dashed lines indicate the range of sunrise and sunset times. Shaded areas refer to the value from the grid box and the neighbouring eight grid boxes. All simulated fluxes are averaged over a whole grid cell, i.e., including urban and vegetation parts

prevailing easterly to south-easterly flow brings cool and humid air from areas covered by vegetation and water bodies, resulting in an increase of the observed value of Q_E (Fig. 5d), which is within that simulated with both model configurations in winter and in summer. Specifically in summer, the simulated latent heat flux shows a wide spectrum of values because of the varying cover fraction of natural surfaces (17%–56%) of the Charlottenburg site and its neighbouring cells. The observed values of Q_E in summer are close to the lower limit of the modelled variability, with some daytime values slightly lower than the simulation. Since we use standard values of plant cover fraction and leaf area index in our simulation, we assume that these values are slightly too large, which results in the overestimation of the modelled Q_E. The current version of the DCEP model neglects the latent heat flux from urban surfaces, so that the grid-cell-averaged values only represent sources in the natural surface part of the grid cell (Schubert 2013). Compared with the DCEP approach, a small amount of indoor latent heat is added by the coupled DCEP–BEM approach (cf. Sect. 3), resulting in similar values for both model runs. The maximum increase of the simulated Q_E by the DCEP–BEM approach compared with the DCEP approach is 8 W m^{-2} at 0900 UTC in winter, and 2 W m^{-2} at 0600 UTC in summer.

6.2 The 2-m Air Temperature and Urban-Heat-Island Intensity

In order to understand the general simulation quality of the CCLM forced by ERA5 reanalysis data, we first evaluate the 2-m air temperature T_{2m} at two rural sites close to Berlin, after which we analyze the UHI intensity ΔT_{UHI} at representative urban and suburban sites in Berlin.

While some studies use the Lindenberg site as a rural site to investigate the UHI effect of Berlin (Schubert and Grossman-Clarke 2013; Trusilova et al. 2016; Jänicke et al. 2017), Lindenberg is not optimally situated with respect to either Alexanderplatz or Buch as it is located 65 km south-east from Alexanderplatz and 75 km south-east from Buch (cf. Fig. 3). Hence, we also consider the Kaniswall site, which is located between Alexanderplatz and Lindenberg and is about 30 km and 35 km south-east from Alexanderplatz and Buch, respectively, as a second reference rural site.

In winter, the observed 2-m air temperature T_{2m}^{OBS} at rural sites varies between −5.4°C and 2.1°C (bold points in Fig. 6a). Specifically, Kaniswall has higher daytime temperatures and lower night-time ones than Lindenberg, resulting in a larger diurnal temperature variation (Kaniswall: 7.5 K, Lindenberg: 6.2 K). The values of T_{2m} at both sites are underestimated in both the DCEP and DCEP–BEM simulations ($m = -1.2$ K at Kaniswall, $m = -1.6$ K at Lindenberg, Table 3). Note that since the DCEP and DCEP–BEM set-ups are designed for urban areas, i.e., where $f_{urb} > 0$ (cf. Table 5 in Appendix 2), there is barely any noticeable difference between the DCEP and DCEP–BEM results for the both rural sites. The simulated Kaniswall 2-m air temperature (red lines in Fig. 6a) is slightly higher than at Lindenberg (blue lines in Fig. 6a); the simulated values at Kaniswall show a considerable underestimation during the day and a relatively good fit during the night. At Lindenberg, this underestimation remains almost constant during the day.

The contrast in 2-m air temperature between both rural sites is more drastic in summer nights (Fig. 6b) when the observed Kaniswall temperature is lower than at Lindenberg, with a difference of up to 3.9 K at 0000 UTC, before reducing around the morning transition. Starting from 0700 UTC, the observed Kaniswall temperature is slightly higher than at Lindenberg. In the afternoon, the observed Kaniswall temperature decreases quicker than the value of Lindenberg. A possible reason is that the Kaniswall weather station is located

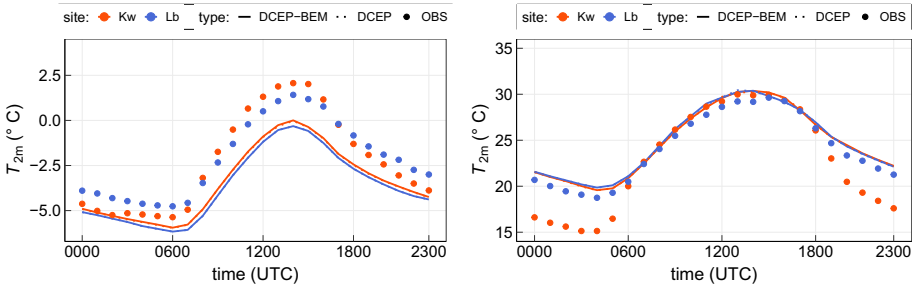

(a) winter **(b)** summer

Fig. 6 Diurnal cycle of the 2-m air temperature at the rural sites Kaniswall (Kw) and Lindenberg (Lb) for the winter period (15 February 2018 0000 UTC to 10 March 2018 2300 UTC) and the summer period (25 July 2018 0000 UTC to 17 August 2018 2300 UTC). Bold points refer to measurements. Dotted and solid lines refer to the DCEP and DCEP–BEM simulations, respectively, where the dotted and solid lines are almost overlapping

Table 3 Root-mean-square error and the MBE of the 2-m temperature (K)

Site	DCEP-WINTER		BEM-WINTER		DCEP-SUMMER		BEM-SUMMER	
	r.m.s.e.	MBE	r.m.s.e.	MBE	r.m.s.e.	MBE	r.m.s.e.	MBE
Kaniswall	2.0	−1.2	2.0	−1.2	3.6	2.1	3.6	2.2
Lindenberg	1.9	−1.6	1.9	−1.6	1.9	0.8	1.8	0.8

far away from larger settlements and in an absolutely flat surrounding so that it develops a very stable atmosphere at night-time. This leads to stronger cooling in the afternoon and at night, resulting in a considerably lower air temperature at night than at Lindenberg. Here, the weather station is situated closer to villages and located on a small hill where cold air may flow downhill, being replaced by warmer near-surface air from above. As even small villages may exhibit the UHI effect (Dienst et al. 2018, 2019), the nocturnal atmosphere at Lindenberg is less stable than that at Kaniswall. In summer at Lindenberg, the model-derived air temperature shows good agreement with observations, with a small overestimation during the night and at noon. While at Kaniswall, the CCLM model considerably overestimates the value of $T_{2\mathrm{m}}$ during the night, where for Lindenberg and Kaniswall, $m = 0.8$ K and 2.1 K, respectively (see Table 3). This contrast results from the inability of CCLM to capture a strong statically stable boundary layer (Schubert and Grossman-Clarke 2014; Mussetti et al. 2020), which is the case at Kaniswall but not at Lindenberg. In this sense, the model better reproduces 2-m air temperature at Lindenberg than at Kaniswall.

Figure 7 exhibits typical spatial distributions of the model-derived $T_{2\mathrm{m}}$ values at about 2 h before sunrise. On average at 0300 UTC in winter (Fig. 7a), the DCEP set-up demonstrates a slight UHI phenomenon of about 1 K, which is more pronounced with the DCEP–BEM set-up (Fig. 7b), i.e., the centre of Berlin is up to 3 K warmer than the surrounding areas. In summer, the contrast of the heat island effect between the DCEP and DCEP–BEM simulation is not evident because the indoor environment is not regulated by the DCEP–BEM approach.

In the following, we define the UHI intensity, $\Delta T_{\mathrm{UHI,Kw/Lb}}$, as the temperature difference between an urban site in Berlin and the reference rural site Kaniswall (Kw) or Lindenberg (Lb),

$$\Delta T_{\mathrm{UHI,Kw/Lb}} = T_{2\mathrm{m,urb}} - T_{2\mathrm{m,Kw/Lb}}. \tag{5}$$

In winter at Alexanderplatz (Fig. 8a), the observed UHI intensity has a clear diurnal cycle with higher values during the night and lower values during the day. Since the value of the observed 2-m air temperature at Kaniswall is higher than that at Lindenberg during the day and lower during the night (see bold points in Fig. 6a), the observed UHI intensity based on Kaniswall $\Delta T^{\mathrm{OBS}}_{\mathrm{UHI,Kw}}$ is lower than the one calculated with Lindenberg $\Delta T^{\mathrm{OBS}}_{\mathrm{UHI,Lb}}$ during the day and higher during the night (Fig. 8a). For instance, whereas the value of $\Delta T^{\mathrm{OBS}}_{\mathrm{UHI,Kw}}$ at Alexanderplatz varies from –0.1 K (1100 UTC) to 2.7 K (0200 UTC), the value of $\Delta T^{\mathrm{OBS}}_{\mathrm{UHI,Lb}}$ ranges from 0.8 K (1100 UTC) to 1.8 K (1900 UTC). The UHI intensity simulated with the DCEP set-up (dotted lines in Fig. 8a) shows a considerable underestimation and has a weak diurnal cycle of 0.2 K (with respect to Kaniswall) or 0.6 K (with respect to Lindenberg). At Alexanderplatz, the value of $\Delta T^{\mathrm{DCEP}}_{\mathrm{UHI,Lb}}$ is predominantly higher than the value of $\Delta T^{\mathrm{DCEP}}_{\mathrm{UHI,Kw}}$ because of the lower DCEP-simulated 2-m air temperature at Lindenberg (see dotted lines in Fig. 6a). The UHI effect with respect to Kaniswall according to the DCEP set-up is less underestimated during the day than the night, but consistently underestimated throughout the day with respect to Lindenberg. In contrast to the observed UHI intensity, which has an

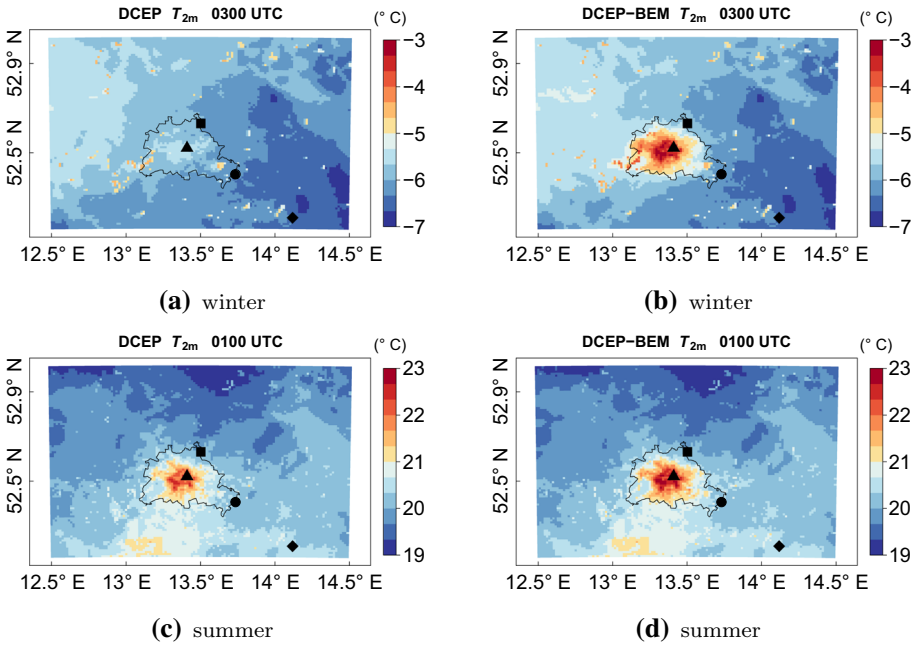

Fig. 7 Typical spatial distribution of the simulated 2-m air temperature T_{2m} at 0300 UTC in winter (**a**, **b**) and at 0100 UTC in summer (**c**, **d**) at a resolution of 1 km. Values are averaged over the whole simulated winter and summer periods, respectively. The area of Berlin is outlined in black. The locations of the urban site Alexanderplatz (triangle), suburban site Buch (square), and rural sites Kaniswall (circle) and Lindenberg (diamond) are also depicted

evident increase during the night, DCEP-derived values only increase slightly after sunset, indicating that the original DCEP approach is not able to reproduce considerable night-time UHI intensity during the winter period. After adding anthropogenic heat from buildings in the DCEP–BEM approach, the modelled UHI intensity at Alexanderplatz increases, especially during the night, so that stronger diurnal cycles are modelled (see solid lines in Fig. 8a). The coupled DCEP–BEM derived UHI intensity at Alexanderplatz varies from 0.4 K (1300 UTC) to 2.0 K (0600 UTC) when calculated with Kaniswall and ranges from 0.7 K (1300 UTC) to 2.2 K (0600 UTC) when calculated with Lindenberg. The r.m.s.e and MBE of the modelled UHI at Alexanderplatz are notably improved when using our coupled DCEP–BEM set-up (see Table 4).

At the suburban site Buch in winter (Fig. 8b), the observed UHI intensity is generally lower than that at Alexanderplatz (Fig. 8a). The observed UHI intensity with respect to Kaniswall at Buch ($\Delta T^{\mathrm{OBS}}_{\mathrm{UHI,Kw}}$ red dotted lines in Fig. 8b) has a clear diurnal cycle with a maximum of 1.3 K at 0200 UTC and a minimum of −0.3 K at 1500 UTC, but with respect to Lindenberg ($\Delta T^{\mathrm{OBS}}_{\mathrm{UHI,Lb}}$ blue dotted lines in Fig. 8b) has a "reversed" diurnal cycle characterized by higher values during the day than during the night.

Compared with the observations, the existing DCEP approach slightly underestimates $\Delta T^{\mathrm{OBS}}_{\mathrm{UHI,Kw}}$ at Buch, particularly during the night, but fails in capturing the "reversed" diurnal cycle of the $\Delta T^{\mathrm{OBS}}_{\mathrm{UHI,Lb}}$ value. This is because the observed value of $T^{\mathrm{OBS}}_{2\mathrm{m}}$ at Buch is higher than at the reference rural site Lindenberg during daytime. As Buch is located 75 km from Lindenberg, the long distances makes the temperature difference due to urban effects less

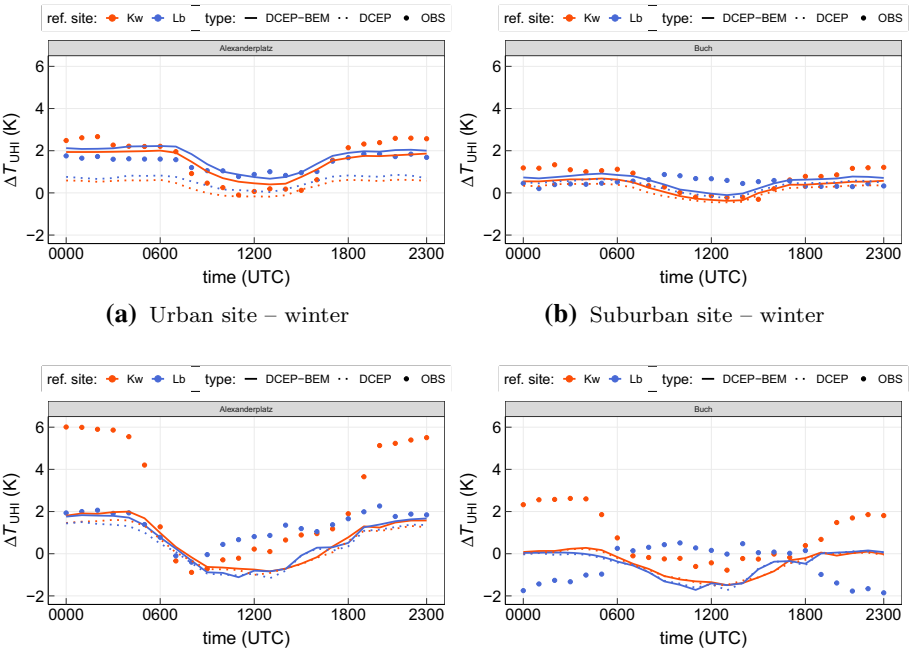

(a) Urban site – winter **(b)** Suburban site – winter

(c) Urban site – summer **(d)** Suburban site – summer

Fig. 8 Averaged diurnal cycle of the UHI intensity (ΔT_{UHI}) at an urban and a suburban site for the simulation periods. Panels **a**, **b** denote the winter period (15 February 2018 0000 UTC to 10 March 2018 2300 UTC) and panels **c**, **d** denote the summer period (25 July 2018 0000 UTC to 17 August 2018 2300 UTC). Bold points refer to measurements. Dotted and solid lines refer to the DCEP and DCEP–BEM simulations, respectively. Values of ΔT_{UHI} are calculated with two reference rural sites: Kaniswall (Kw, red) and Lindenberg (Lb, blue)

pronounced than due to the geographical locations. The increased UHI intensity with respect to Kaniswall according to the DCEP–BEM approach for Buch (solid lines in Fig. 8b) is not as evident as for Alexanderplatz (solid lines in Fig. 8a), owing to the low value of f_{urb} and the dominant low-rise buildings of the grid cell in which Buch is located (cf. Table 5 in Appendix 2). The r.m.s.e. and MBE are slightly improved by the DCEP–BEM set-up for Buch (see Table 4), with both DCEP and DCEP–BEM approaches capable of capturing the night-time UHI at Buch in winter.

In summer, the observed UHI intensity at Alexanderplatz remains constant during the night and drops during the morning transition (bold points in Fig. 8c), with negative values observed from 0700 UTC to 0900 UTC. Several hours after sunrise, the observed UHI intensity begins to rise again, when the value of $\Delta T^{\mathrm{OBS}}_{\mathrm{UHI,Kw}}$ exceeds 6.0 K around midnight, whereas the maximum value of $\Delta T^{\mathrm{OBS}}_{\mathrm{UHI,Lb}}$ is only 2.1 K. At Alexanderplatz, the UHI intensity modelled by the DCEP approach has a larger daily variation in summer (dotted lines in Fig. 8c) than in winter (dotted lines in Fig. 8a), with summer values ranging from -1.0 K to 1.6 K with respect to Kaniswall and -1.2 K to 1.5 K when calculated with Lindenberg. Negative values of the DCEP derived ΔT_{UHI} occur in both cases between 0700 UTC and 1600 UTC. Compared with the DCEP approach, the UHI intensity modelled by the coupled DCEP–BEM approach does not increase considerably in summer (see solid lines in Fig. 8c), meaning these models

Table 4 Change of r.m.s.e and MBE of ΔT_{UHI} in kelvin when comparing the DCEP–BEM with the DCEP approaches

Period	Reference rural site	Alexanderplatz		Buch	
		r.m.s.e	MBE	r.m.s.e	MBE
Winter	Kaniswall	−0.7	−1.0	0.0	−0.2
	Lindenberg	−0.4	−0.8	0.0	−0.1
Summer	Kaniswall	−0.2	−0.2	0.0	0.0
	Lindenberg	0.0	−0.2	0.0	0.0

Negative values indicate improvements by the DCEP–BEM approach

have similar performances at Alexanderplatz in summer with a comparable r.m.s.e and MBE (see Table 4).

At Buch in summer (Fig. 8d), whereas the values of $\Delta T^{\mathrm{OBS}}_{\mathrm{UHI,Kw}}$ vary from −0.8 K to 2.6 K with higher values during the night, the values of $\Delta T^{\mathrm{OBS}}_{\mathrm{UHI,Lb}}$ show a "reversed" diurnal pattern, with the highest values occurring during the day. This results from higher and lower $T^{\mathrm{OBS}}_{\mathrm{2m}}$ values at Buch compared with at Lindenberg from 0600 UTC to 1800 UTC and at night, respectively. In this case, the value of $T^{\mathrm{OBS}}_{\mathrm{2m}}$ at the rural site is higher at night-time than the suburban site because Buch is lies north-west of Lindenberg, and there is a dominant cold airflow from the north near the surface during the simulation period. The value of $\Delta T^{\mathrm{DCEP}}_{\mathrm{UHI,Kw}}$ at Buch (the red dotted line in Fig. 8d) has a similar diurnal cycle to the observations but is considerably underestimated ($m = -1.3$ K). Again, the "reversed" diurnal cycle of $\Delta T^{\mathrm{OBS}}_{\mathrm{UHI,Lb}}$ values is not reproduced by the DCEP and DCEP–BEM approaches. Compared with the DCEP results, values of the UHI intensity modelled with the DCEP–BEM approach do not show considerable difference at Buch in summer.

6.3 Indoor Temperature During the Summer Period

The observed indoor temperature range at Rothenburg and Kigaramler of 23.2–32.7 °C and 26.3–35.0 °C, respectively (see the black lines in Fig. 9), is smaller than the corresponding outdoor 2-m temperature (see the yellow lines in Fig. 9). This difference mainly results from the different locations of indoor temperature sensors (cf. Sect. 5.3). The peak of the observed indoor temperature usually occurs 1–2 h later than the peak of the observed 2-m air temperature because the indoor temperature has a delayed response with respect to the outdoor temperature due to the thermal inertia of buildings.

The grey shaded areas in Fig. 9 denote all possible indoor temperatures at each story simulated with the DCEP–BEM approach, including four street directions and two room orientations. At Rothenburg (Fig. 9a), the simulated indoor temperature lies within the range of the observed values for 14 days and slightly overestimates it for the other days, in particular during the periods with marked drops in temperature. There are two possible reasons for this. Firstly, the building at Rothenburg is relatively small and without neighbouring buildings, resulting in a faster thermal response than the street canyons assumed in the DCEP–BEM set-up. Secondly, the sensor is positioned on the north side of the room and receives little sunshine. Nevertheless, the model is able to capture the general behaviour of the indoor temperature at Rothenburg.

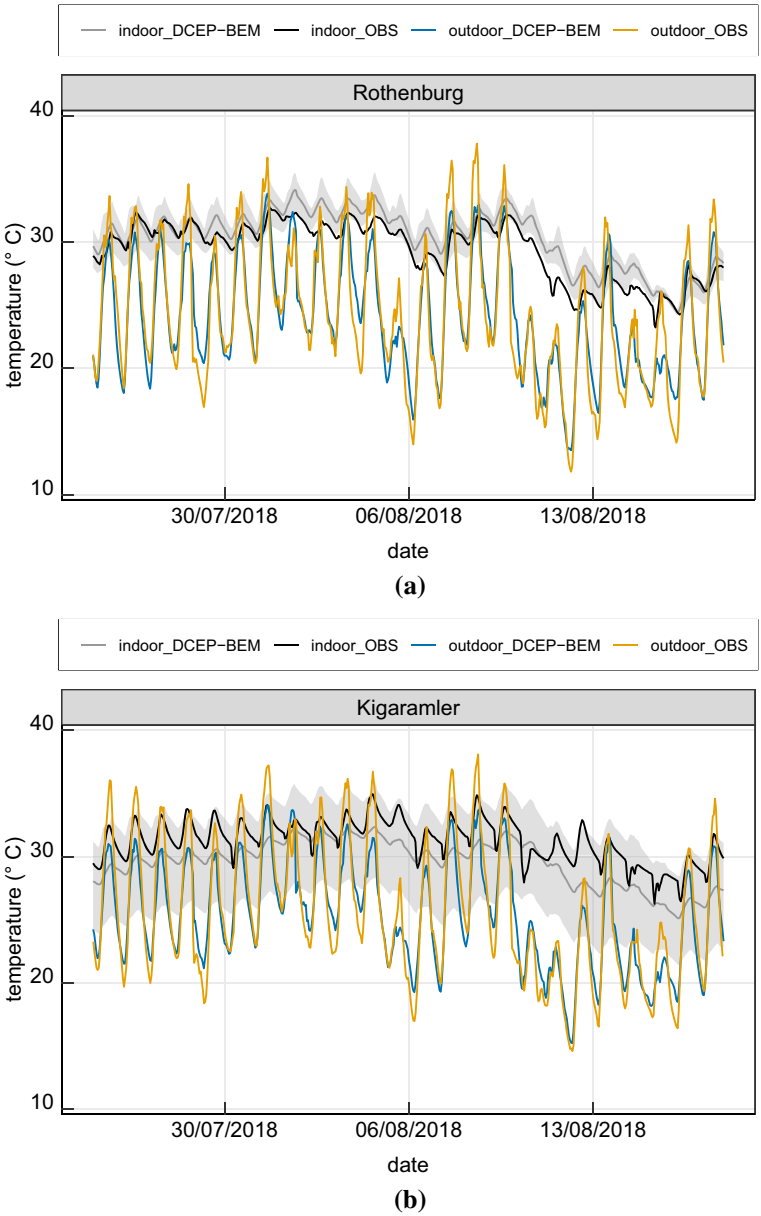

Fig. 9 Time series of indoor and outdoor air temperature at Rothenburg (**a**) and Kigaramler (**b**) for the summer period (25 July 2018 0000 UTC to 17 August 2018 2300 UTC). Yellow lines represent the observed outdoor 2-m temperature, blue lines indicate the DCEP–BEM derived 2-m temperature, and black lines denote the observed indoor temperature. Grey shaded regions and grey solid lines depict the simulated indoor temperature range of the DCEP–BEM approach and the mean simulated indoor temperature, respectively. Four street directions and two room orientations are included

At Kigaramler (Fig. 9b), due to the higher urban fraction and building height of the grid cell (cf. Table 5 in Appendix 2), the modelled indoor temperature has a wider range than at Rothenburg and is found within the range of indoor observations for the whole period.

6.4 Energy Consumption for Heating During the Winter Period

For the winter simulation, the energy consumption for heating is calculated with the coupled DCEP–BEM approach. Figure 10 shows the spatial distribution of the energy consumption E_C averaged over the winter period. The mean and maximum values of E_C for the entire area of Berlin are $8\,W\,m^{-2}$ and $34\,W\,m^{-2}$, respectively, with large values of E_C ($> 20\,W\,m^{-2}$) mainly occurring in the central areas.

To investigate the influencing factors of the modelled-derived energy consumption, we present the time series for the urban site Alexanderplatz and the suburban site Buch during the winter period (Fig. 11), with both sites yielding a reduced 2-m temperature according to the model from 23 February 2018 to 4 March 2018, whereas the energy consumption shows a considerable increase concurrently; i.e., the value of E_C increases along with a decrease in temperature. At Buch, the energy consumption $E_C = 2 - 7\,W\,m^{-2}$, with a mean value for the entire period $\overline{E_C} = 4\,W\,m^{-2}$, while at Alexanderplatz, $E_C = 8 - 24\,W\,m^{-2}$, with a mean value $\overline{E_C} = 15\,W\,m^{-2}$, which is about three times larger than that at Buch. Note that since the calculated energy consumption is averaged over the urban and non-urban part of a grid cell, the urban fraction of a grid cell and its building distribution is the main factor that influences the energy consumption of that cell.

Various studies have estimated the energy consumption for space heating in winter, with some using the term "anthropogenic heat flux" to include the emissions from building heating, traffic, or industry. Karsisto et al. (2016) estimated an anthropogenic heat flux of $42\,W\,m^{-2}$ in January for a dense city-centre site in the high-latitude city Helsinki, Finland. A similar value ($50\,W\,m^{-2}$) was obtained from measurements at the same site by Nordbo et al. (2013). These values are much larger than our values at Alexanderplatz because the air temperature in Helsinki in winter is much lower than in Berlin and the studies of Helsinki include traffic and industrial activities as well.

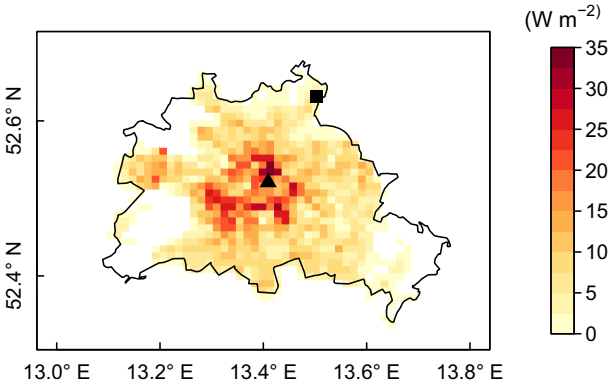

Fig. 10 Spatial distribution of the mean energy consumption E_C for the winter period (15 February 2018 0000 UTC to 10 March 2018 2300 UTC). The city border of Berlin is outlined with the black line. The locations of the urban site Alexanderplatz (triangle) and suburban site Buch (square) are also depicted. Each pixel value represents the energy consumption averaged for a grid cell

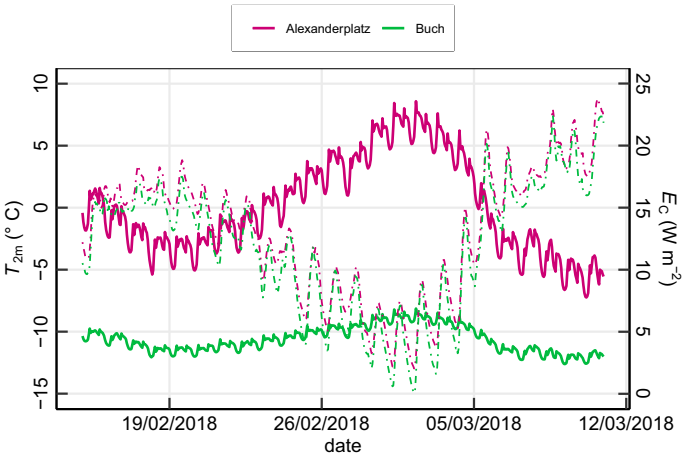

Fig. 11 Time series of the DCEP–BEM derived 2-m air temperature T_{2m} (dot-dashed lines) and energy consumption E_C (solid lines) at the urban site Alexanderplatz and the suburban site Buch for the winter simulations (15 February 2018 0000 UTC to 10 March 2018 2300 UTC)

In order to compare the energy consumption between grid cells regardless of different building parameters, we consider only the urban part of a grid cell and compute the energy consumption per floor area $E_{C,floor}$ as

$$E_{C,floor} = \frac{E_{C,tot}}{BDN_{floor}} = \frac{E_{C,tot}/D}{BN_{floor}}, \tag{6}$$

with the total energy consumption $E_{C,tot}$ (W) of a building and the number of the floors N_{floor} of a building. Note that the parameter E_{tot}/D is the output quantity of the model because of the limit $D \to \infty$ employed.

The value of $E_{C,floor}$ at Alexanderplatz (the magenta line in Fig. 12a) ranges from 12 W m^{-2} to 14 W m^{-2} with the maximum occurring at 0800 UTC and 1900 UTC, and the minimum occurring in the early morning before sunrise. The diurnal cycle of the energy consumption E_C roughly follows the pattern of the target indoor temperature (cf. Fig. 4).

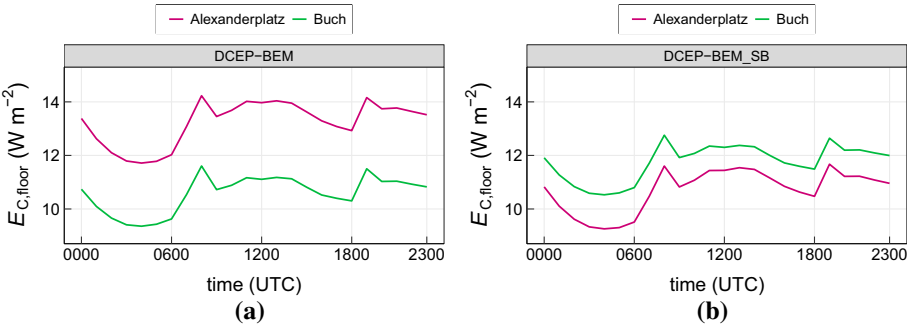

Fig. 12 Averaged diurnal cycle of the energy consumption per floor area $E_{C,floor}$ at the urban site Alexanderplatz (red) and the suburban site Buch (green) for the winter simulations (15 February 2018 0000 UTC to 10 March 2018 2300 UTC). The results in (**a**) show the standard run and the results in (**b**) present the run with spatially-constant street and building widths

Around midnight, its value decreases sharply along with the target indoor temperature. From 0600 UTC, its value starts increasing and reaches the maximum at 0800 UTC. At 0900 UTC, even though the target indoor temperature further increases, its value decreases by $0.8\,\mathrm{W\,m^{-2}}$ because of the strong increase in air temperature (0.7 K, not shown). Afterwards, the values increase slightly but not as much as at 0800 UTC because the increasing air temperature reduces the energy consumption. From 1400 UTC to 1800 UTC, the value of $E_{\mathrm{C,floor}}$ decreases together with the target indoor temperature. At 1900 UTC, the second peak values occurs because the target indoor temperature at 1900 UTC is slightly higher than at 1800 UTC and the air temperature drops by 0.4 K in the meantime. A similar diurnal patter for winter days has been reported in Moriwaki et al. (2008) and Dong et al. (2017).

The model-derived value of $E_{\mathrm{C,floor}}$ at Buch (the green line in Fig. 12a) has a similar diurnal cycle and a considerably decrease by 20%, compared with at Alexanderplatz. This behaviour is contrary to our expectation that the UHI effect, which is larger at Alexanderplatz, reduces the energy demand for heating. The reason for the opposite behaviour in our case is that the building width at Alexanderplatz is smaller than at Buch by $> 30\%$, which leads to a larger building-surface-to-building-interior ratio per floor and a larger value of $E_{\mathrm{C,floor}}$ at Alexanderplatz.

The urban canopy parameters for building width and urban fraction are chosen such that the fraction of buildings and impervious surfaces in the model correspond to that in reality (Schubert and Grossman-Clarke 2013). Thus, in order to reduce the effect of different urban canopy parameters on the value of $E_{\mathrm{C,floor}}$, we conduct an additional simulation in which the building widths and the street widths of all grid cells are set to 17 m and 25 m, respectively. The building heights remain the same as in the default setting in order to reproduce the UHI effect sufficiently well. With these parameters (Fig.12b), we find that the value of $E_{\mathrm{C,floor}}$ at Buch is 10% higher than at Alexanderplatz, indicating a potential energy saving due to the UHI effect at the urban site Alexanderplatz. Paolini et al. (2017) reported a reduction of the energy consumption for heating of 16% for the urban buildings resulting from the UHI effect in Milan, Italy. Similarly in Modena, Italy, about 19%–20% less heating energy was required for a building located in the urban area than in a suburban area (Magli et al. 2015).

Since the daily consumed energy estimated in Sect. 5.4 is based on the building plan area, we derive the corresponding simulated values by dividing the energy consumption of a grid cell from Fig. 10 by the urban fraction of that grid cell. This yields a spatial average of $0.47\,\mathrm{kW\,h\,m^{-2}}$, which reduces by the same order of magnitude and is comparable to the average values ($0.73\,\mathrm{kW\,h\,m^{-2}}$ for February and $0.63\,\mathrm{kW\,h\,m^{-2}}$ for March).

7 Conclusion

The BEM approach based on Salamanca et al. (2010) is developed for the urban canopy model DCEP and coupled with the mesoscale climate model CCLM. By enforcing target indoor temperatures, the new coupled approach dynamically computes the evolution of anthropogenic heating of the building interior and the heat exchange with the outdoor environment. Four simulations of 24 days duration each, consisting of two reference runs with the existing CCLM/DCEP approach and two runs applying the improved model with the BEM approach, are conducted for a winter and a summer period in 2018 for Berlin, Germany. In winter, as buildings are equipped with heating systems, energy consumption in the urban area and the link between the indoor heat load onto the UHI are explored. In summer, considering the low percentage of air conditioning installed in private households in Berlin, indoor temperature

and its response to outdoor air temperature is investigated. Model runs are evaluated using multiple datasets of indoor and outdoor air temperature, and turbulent heat fluxes.

While in summer, the reference DCEP approach and improved BEM approach are able to realistically model surface sensible heat and latent heat fluxes, the reference underestimates sensible heat fluxes in winter. With the consideration of anthropogenic heat emissions, the coupled BEM approach produces realistic sensible heat fluxes in both summer and winter.

Consequently, in winter, our strategy considerably improves the calculation of T_{2m} values compared with the existing model lacking the BEM approach. In summer, since additional heat loading due to air conditioning is not considered for our Berlin case, there is not much difference in T_{2m} values between the reference and modified approaches. The UHI intensity ΔT_{UHI} is calculated to quantitatively analyze the UHI effect, which includes two rural sites for its calculation because the choice of the rural site has a distinct influence on the UHI intensity. In winter, the observed UHI intensity calculated with both rural sites shows the classic diurnal cycle with higher values during the night and lower values during daytime and is qualitatively captured by both reference and improved models; however, the reference DCEP model underestimates the UHI intensity with a large MBE at Alexanderplatz. The coupled DCEP–BEM approach remarkably reduces the MBE of the UHI effect at Alexanderplatz by 1.0 K and 0.8 K, calculated with Kaniswall and Lindenberg sites, respectively, and it is slightly improved at Buch site. In summer, the night-time ΔT_{UHI} values at the urban site Alexanderplatz are well reproduced by both the reference DCEP and coupled BEM approaches when ΔT_{UHI} is calculated based on the rural site Lindenberg. Both models, however, underestimate the night-time ΔT_{UHI} value by up to 4 K compared with the observed value calculated using Kaniswall as the rural site. The suburban site Buch shows a reversed UHI signal during the diurnal cycle when calculated with one rural site (Lindenberg), while with the other site (Kaniswall) the diurnal cycle follows the classic pattern. This reversed pattern is not reproduced by both model runs. Similar to the parameter T_{2m}, the difference in ΔT_{UHI} values between the two model runs is negligible in summer.

The indoor temperature during the summer period strongly depends on the building and its surroundings, room orientation, and the location of the measuring devices. Nonetheless, the evaluation with respect to the measurements confirms the capability of the coupled BEM approach to simulate indoor temperature during summer.

During the winter, the simulated energy consumption for the entire area of Berlin is $8\,W\,m^{-2}$ on average, with the maximum values occurring in the central areas, where buildings are higher and denser than in surrounding areas. The model-derived daily consumed energy is $0.47\,kW\,h\,m^{-2}$ per floor area, which falls by the same order of magnitude and is comparable to the average values estimated from other sources for February ($0.73\,kW\,h\,m^{-2}$) and for March ($0.63\,kW\,h\,m^{-2}$). The coupling effect of building energy consumption and air temperature is also addressed, finding that, in areas with more urban structures or during periods with lower temperatures, more energy is consumed for indoor space heating.

We find that energy consumption is also linked to target indoor temperature: during the daytime, more energy is consumed than during the night. The energy consumption per floor area at the suburban site is up to $2\,W\,m^{-2}$ (20%) less than at the urban site. An additional analysis with spatially constant building widths and street widths is conducted and it shows that, compared with the urban site, the suburban site displays a 10% increase in energy consumption, implying a potential energy saving due to the UHI effect. We find that the building width has an essential effect on the estimation of energy consumption.

To conclude, coupling of the BEM approach in an urban climate model is worthwhile for a more realistic and accurate representation of near-surface energy fluxes and air temperature

in mid-latitude cities. This is especially the case for winter simulations, when space heating constitutes a large part of anthropogenic heat emissions.

Acknowledgements Luxi Jin was funded by the German Research Foundation (DFG) as part of the research project "Heatwaves in Berlin, Germany – climate projections" (Grant No. SCHU 3191/1-1). Daniel Fenner received financial support from DFG as part of the research project "Heat waves in Berlin, Germany – urban climate modifications" (Grant No. SCHE 750/15-1). We thank all Netatmo owners who shared their data. We further thank Tom Grassmann for support with CWS data, and Hartmut Küster and Ingo Suchland for maintaining the weather stations of the Technical University of Berlin. The authors declare no conflict of interest.

Funding Open Access funding provided by Projekt DEAL.

Appendix 1: Supplementary Equations for the Enhancements of the Urban Scheme

This section provides supplementary equations for Sect. 2.1. The limit $D \to \infty$ in the latest DCEP version is carried out by applying the limit $b \to \infty$ of the basic view factors for two parallel and rectangular surfaces, $f_{\mathrm{prl}}(a, b, c)$ and $f_{\mathrm{nrm}}(a, b, c)$, respectively, described in Martilli et al. (2002), where a, b, and c are the dimensions of the respective surfaces. We find

$$\begin{aligned}
\lim_{b\to\infty} f_{\mathrm{prl}}(a,b,c) = \lim_{b\to\infty} \frac{2}{\pi}\Bigg(& \frac{c^2}{2ab} \ln \frac{(a^2+c^2)(b^2+c^2)}{c^2(a^2+b^2+c^2)} \\
& + \frac{\sqrt{a^2+c^2}}{a} \arctan \frac{b}{\sqrt{a^2+c^2}} \\
& + \frac{\sqrt{b^2+c^2}}{b} \arctan \frac{a}{\sqrt{b^2+c^2}} \\
& - \frac{c}{a} \arctan \frac{b}{c} - \frac{c}{b} \arctan \frac{a}{c} \Bigg) \\
= \frac{1}{a}\left(\sqrt{a^2+c^2} - c\right), & \qquad (7) \\
\lim_{b\to\infty} f_{\mathrm{nrm}}(a,b,c) = \lim_{b\to\infty} \frac{1}{\pi}\Bigg[& \frac{1}{4}\Bigg(\frac{b}{c} \ln \frac{(a^2+b^2)(b^2+c^2)}{b^2(a^2+b^2+c^2)} \\
& + \frac{a^2}{bc} \ln \frac{a^2(a^2+b^2+c^2)}{(a^2+c^2)(a^2+b^2)} \\
& + \frac{c}{b} \ln \frac{c^2(a^2+b^2+c^2)}{(a^2+c^2)(b^2+c^2)} \Bigg) \\
& + \arctan \frac{b}{c} + \frac{a}{c} \arctan \frac{b}{a}
\end{aligned}$$

$$- \frac{\sqrt{a^2+c^2}}{c} \arctan \frac{b}{\sqrt{a^2+c^2}} \Bigg] = \frac{1}{2c}\left(a + c - \sqrt{a^2+c^2}\right). \tag{8}$$

The view factors for radiation from an infinitesimal area to a finite area described in Schubert et al. (2012) and Schubert (2013), $f^{\mathrm{d}}_{\mathrm{prl}}(a,b,c)$ and $f^{\mathrm{d}}_{\mathrm{nrm}}(a,b,c)$, are adjusted as

$$\begin{aligned}\lim_{b\to\infty} f^{\mathrm{d}}_{\mathrm{prl}}(a,b,c) &= \lim_{b\to\infty} \frac{1}{\pi}\left(\frac{\sqrt{b^2+c^2}}{b} \arctan \frac{a}{\sqrt{b^2+c^2}} \right.\\ &\quad \left. - \frac{c}{b}\arctan\frac{a}{c} + \frac{a}{\sqrt{a^2+c^2}} \arctan \frac{b}{\sqrt{a^2+c^2}}\right)\\ &= \frac{1}{2}\frac{a}{\sqrt{a^2+c^2}}, \end{aligned} \tag{9}$$

$$\begin{aligned}\lim_{b\to\infty} f^{\mathrm{d}}_{\mathrm{nrm}}(a,b,c) &= \lim_{b\to\infty} \frac{1}{\pi}\left(\arctan\frac{b}{c} + \frac{c}{2b}\ln\frac{c^2(a^2+b^2+c^2)}{(b^2+c^2)(a^2+c^2)} \right.\\ &\quad \left. - \frac{c}{\sqrt{a^2+c^2}} \arctan \frac{b}{\sqrt{a^2+c^2}}\right)\\ &= \frac{1}{2}\left(1 - \frac{c}{\sqrt{a^2+c^2}}\right). \end{aligned} \tag{10}$$

Furthermore, based on the results of Santiago and Martilli (2010) and Krayenhoff et al. (2015), we use increased drag coefficients of wall surfaces C_{W} depending on the building plan area density $\lambda_{\mathrm{p}} = B/(W+B)$,

$$C_{\mathrm{W}} = \begin{cases} 3.67 & \text{for } \lambda_{\mathrm{p}} > 0.33 \\ 7.30\lambda_{\mathrm{p}}^{0.62} & \text{for } \lambda_{\mathrm{p}} \le 0.33 \end{cases}. \tag{11}$$

The original formulation used a value of $C_{\mathrm{W}} = 0.4$.

Appendix 2: Climatological Background and Site Information

Table 5 Urban parameters of the model grid cells in which urban sites are located. γ_i: building height distribution

Site	f_{urb}	W/m	B/m	γ_i						
				0 m	5 m	10 m	15 m	20 m	25 m	30 m
Alexanderplatz	0.69	29.80	14.70	0.00	0.03	0.02	0.04	0.19	0.41	0.26
Buch	0.39	35.30	19.50	0.01	0.12	0.25	0.32	0.23	0.00	0.02
Kigaramler	0.64	14.80	6.60	0.00	0.04	0.02	0.17	0.70	0.07	0.00
Kaniswall	0.00	0.00	0.00	0.00	0.00	0.00	0.00	0.00	0.00	0.00
Lindenberg	0.00	0.00	0.00	0.00	0.00	0.00	0.00	0.00	0.00	0.00
Rothenburg	0.44	17.10	9.10	0.00	0.08	0.20	0.31	0.39	0.01	0.00
Charlottenburg	0.81	21.50	17.50	0.00	0.01	0.04	0.09	0.36	0.50	0.00

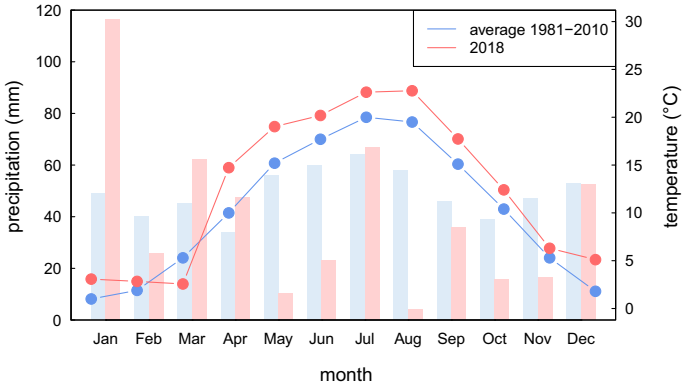

Fig. 13 Climate diagram for the Berlin-Alexanderplatz site for the period 1981–2010 (blue line and bars) and the year 2018 (red line and bars); lines: mean daily 2-m air temperature; bars: monthly sum of precipitation

Appendix 3: Measurement of Radiative and Turbulent Heat Flux at the Charlottenburg Site

At the Charlottenburg site, total downwards shortwave and longwave radiation data are measured by a CNR4 net radiometer (Kipp & Zonen, Delft, The Netherlands) with integrated ventilation, and the diffuse downwards shortwave radiation is measured by a SPN1 sunshine pyranometer (Delta-T Devices, Cambridge, UK), at 1-min resolution. Shortwave radiation data at Charlottenburg is quality controlled by removing data during precipitation events, correcting for the night-time offset, and removing negative daytime values as well as values $> 1230\,\mathrm{W\,m^{-2}}$. Diffuse downwards shortwave radiation data are omitted if values are larger than the total downwards shortwave radiation. Longwave radiation data outside the range $[150\,\mathrm{W\,m^{-2}}, 500\,\mathrm{W\,m^{-2}}]$ are excluded. After quality control, all radiation data at Charlottenburg are aggregated to hourly mean values.

Data quality control and processing of turbulent heat flux data with EddyPro include the elimination of spikes, filtering values based on physical thresholds, and statistical screening based on the method developed by Vickers and Mahrt (1997). We apply double coordinate rotation, correction of sonic temperature for humidity, high- and low-frequency spectral corrections (Moncrieff et al. 1997), and corrections for air density (Webb et al. 1980). Furthermore, instrument diagnostic flags not equal to zero and data with signal strength < 0.8 are withheld. Any data at 30-min resolution with quality flag of 2 are excluded (Foken 2016; Mauder and Foken 2011) as well as if precipitation is observed (Laser precipitation monitor, Thies CLIMA) at Charlottenburg within the respective interval. Additionally, data within the wind directions of 17° to 35° are excluded because this sector is influenced by flow distortion due to the instrument and mounting set-up (Foken 2016).

Appendix 4: Evaluation of Shortwave and Longwave Radiation at Observational Sites

The simulation performance of shortwave (SW) and longwave (LW) radiation is evaluated using the maximum absolute deviation which describes the maximum difference of two

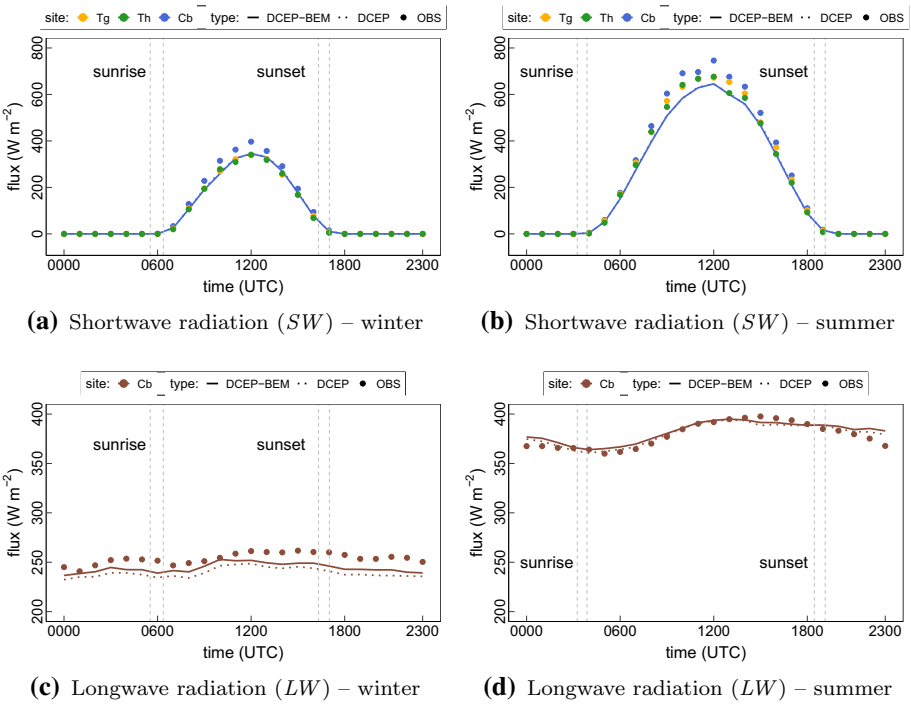

(a) Shortwave radiation (SW) – winter **(b)** Shortwave radiation (SW) – summer

(c) Longwave radiation (LW) – winter **(d)** Longwave radiation (LW) – summer

Fig. 14 Averaged diurnal cycle of radiative fluxes (SW and LW) at the Charlottenburg site (Cb) for the simulation periods. The panels **a**, **c** denote the winter period (15 February 2018 0000 UTC to 10 March 2018 2300 UTC) and the panels **b**, **d** denote the denotes the summer period (25 July 2018 0000 UTC to 17 August 2018 2300 UTC). Bold points refer to measurements (OBS). Dotted and solid lines refer to the DCEP and DCEP–BEM simulations, respectively. Vertical grey dashed lines indicate the range of sunrise and sunset times. Additionally, measurements of SW from the DWD sites Tegel (Tg) and Tempelhof (Th) are used as reference in (**a**) and (**b**). All simulated fluxes are averaged over a whole grid cell, i.e., including urban and vegetation part

datasetes by

$$s = \max\{|X_{1,\ldots,n} - Y_{1,\ldots,n}|\}, \tag{12}$$

where X, Y are two different datasets, and n is the number of samples, and the mean deviation describing the mean difference of two datasets is

$$d = \frac{1}{n}\sum_{i=1}^{n}(X_i - Y_i), \tag{13}$$

Figure 14a,b displays the averaged diurnal cycle of shortwave radiation at different sites. In addition to the Charlottenburg site, hourly shortwave radiation data from two additional measurement sites nearby (Tegel[3] and Tempelhof[4]) by the German Meteorological Service (DWD)[5] are also used.

[3] 52.56°N,13.31°E.

[4] 52.47°N,13.40°E.

[5] Source of data: Climate Data Center OpenData operated by DWD (https://opendata.dwd.de/climate_environment/CDC/).

Table 6 Maximum absolute deviation (MAD) (first number) and mean deviation MD (second number) of shortwave (SW) and longwave radiation (LW) in $\mathrm{W\,m^{-2}}$ based on the winter (WIN) and summer (SUM) periods. Columns labelled "Difference in measurements" describe the difference among three sites. Columns labelled "Improvement by DCEP–BEM" show the difference between the DCEP–BEM and DCEP approaches. Positive values within "Improvement by DCEP–BEM" indicate an improvement compared with the DCEP approach. Negative values indicate a deterioration in performance. The table provides a summary of Fig. 14a,b

	Difference in measurement MAD / MD			Improvement by DCEP–BEM MAD / MBE		
	Observations			Simulations		
	Cb-Tg	Cb-Th	Tg-Th	Cb	Tg	Th
SW-WIN	59/14	56/15	12/1	-3/0	4/1	-3/1
SW-SUM	74/16	69/23	48/7	2/-1	0/-1	2/-1
LW-WIN	–	–	–	4/4	–	–
LW-SUM	–	–	–	-3/-2	–	–

During the winter period (Fig. 14a), the observed shortwave radiation at the DWD sites Tegel and Tempelhof are similar ($d = 1\,\mathrm{W\,m^{-2}}$, see Table 6) and smaller than that observed at Charlottenburg (blue bold points in Fig. 14a). The deviation of the observations between Charlottenburg and the two DWD sites increases from the morning transition until 1200 UTC with a maximum absolute deviation $s = 59\,\mathrm{W\,m^{-2}}$ and then decreases. In summer (Fig. 14b), the difference in the observations is more evident among three sites. The maximum absoblute deviation between the Charlottenburg and Tegel sites occurs at 1400 UTC ($s = 74\,\mathrm{W\,m^{-2}}$). Again, the difference in the observations between Charlottenburg and the two DWD sites ($d = 16\,\mathrm{W\,m^{-2}}$ with Tegel and $d = 23\,\mathrm{W\,m^{-2}}$ with Tempelhof, see Table 6) is still larger than the difference between the two DWD sites ($d = 7\,\mathrm{W\,m^{-2}}$). This contrast may result from different sensors of diverse networks and alternated cloud cover at different locations. A further analysis of diffuse shortwave radiation (not shown) confirms the ability of the model to simulate diffuse shortwave radiation and implies that more direct shortwave radiation is measured at Charlottenburg than the other two sites.

In winter, the DCEP and DCEP–BEM derived shortwave radiation show a good agreement with the observations at the two DWD sites but a large underestimation at Charlottenburg. More specifically, the MBE by the DCEP approach at Tegel, Tempelhof and Charlottenburg is $2\,\mathrm{W\,m^{-2}}$, $3\,\mathrm{W\,m^{-2}}$, and $-12\,\mathrm{W\,m^{-2}}$, respectively (see Table 6). The DCEP–BEM approach shows a similar performance of the shortwave radiation with regard to the r.m.s.e and the MBE. In summer at Tegel and Tempelhof, in contrast to the good fit in the winter case, an underestimation with an average of up to $-19\,\mathrm{W\,m^{-2}}$ is produced. A possible reason is that during summer CCLM overestimates the scattering and absorption of radiation in the overlaying atmosphere, leading to higher values of diffuse radiation and lower values for direct radiation. Similar to winter, the DCEP and DCEP–BEM derived shortwave radiation at the Charlottenburg site again show larger differences from observations than at the other sites in summer. The mean absolute deviation and MBE at Charlottenburg are around twice as large as at the sites Tegel and Tempelhof (see Table 6).

The observed downwards longwave radiation at Charlottenburg fluctuates at around $250\,\mathrm{W\,m^{-2}}$ in winter with a weak diurnal pattern (see Fig. 14c), but shows a more clear diurnal pattern in summer with a maximum of $398\,\mathrm{W\,m^{-2}}$ at 1500 UTC and a minimum of $360\,\mathrm{W\,m^{-2}}$ at 0500 UTC (see Fig. 14d). In winter, the DCEP approach underestimates the longwave radiation with a negative MBE, $m = -14\,\mathrm{W\,m^{-2}}$ (not shown). The DCEP–

BEM approach improves the estimate of the longwave radiation by reducing the MBE by $4\,\mathrm{W\,m^{-2}}$. In summer, both the DCEP and DCEP–BEM derived longwave radiation are close to the observations, with $m = 1\,\mathrm{W\,m^{-2}}$ and $3\,\mathrm{W\,m^{-2}}$, respectively (not shown).

To conclude, both the DCEP and DCEP–BEM approaches estimate both the shortwave and longwave radiation well, because the calculation of radiative fluxes in CCLM is barely influenced by building structures.

References

Berlin, Senate Department for Urban Development and Housing (2010) 08.01 Versorgungsbereiche Gebäudewärme / 08.02 Überwiegende Heizungsarten (in German). Berlin, Senate Department for Urban Development and Housing, Berlin, Tech Rep

Bohnenstengel SI, Hamilton I, Davies M, Belcher SE (2014) Impact of anthropogenic heat emissions on London's temperatures. Q J R Meteorol Soc 140(679):687–698

Bueno B, Norford L, Pigeon G, Britter R (2011) Combining a detailed building energy model with a physically-based urban canopy model. Boundary-Layer Meteorol 140(3):471–489

Bureau of Statistics Berlin-Brandenburg (2019) Wohnfläche je Einwohner in Berlin (in German). Bureau of Statistics Berlin-Brandenburg, Tech rep

Chow WTL, Salamanca F, Georgescu M, Mahalov A, Milne JM, Ruddell BL (2014) A multi-method and multi-scale approach for estimating city-wide anthropogenic heat fluxes. Atmos Environ 99:64–76

Chrysoulakis N, Grimmond CSB (2016) Understanding and reducing the anthropogenic heat emission. In: Kolokotsa D, Santamouris M (eds) Urban climate mitigation techniques. Routledge, London, pp 27–40

Copernicus Climate Change Service (2017) Fifth generation of ECMWF atmospheric reanalyses of the global climate

Crawley DB, Lawrie LK, Winkelmann FC, Buhl WF, Huang YJ, Pedersen CO, Strand RK, Liesen RJ, Fisher DE, Witte MJ, Glazer J (2001) EnergyPlus: creating a new-generation building energy simulation program. Energy Build 33(4):319–331

Davies HC (1976) A lateral boundary formulation for multi-level prediction models. Q J R Meteorol Soc 102(432):405–418

Dienst M, Lindn J, Esper J (2018) Determination of the urban heat island intensity in villages and its connection to land cover in three european climate zones. Clim Res 76

Dienst M, Lindn J, scar S, Esper J (2019) Detection and elimination of UHI effects in long temperature records from villages A case study from Tivissa, Spain. Urban Clim 27:372–383

Doms G, Förstner J, Heise E, Herzog HJ, Mironov D, Raschendorfer M, Reinhardt T, Ritter B, Schrodin R, Schulz JP, Vogel G (2018) A Description of the Nonhydrostatic Regional COSMO Model (COSMO V5.05): PART II Physical Parametrizations. Consortium for Small-scale Modeling, Tech rep

Dong Y, Varquez AC, Kanda M (2017) Global anthropogenic heat flux database with high spatial resolution. Atmos Environ 150:276–294

Erell E, Williamson T (2007) Intra-urban differences in canopy layer air temperature at a mid-latitude city. Int J Climatol 27(9):1243–1255

Fan H, Sailor DJ (2005) Modeling the impacts of anthropogenic heating on the urban climate of Philadelphia: a comparison of implementations in two PBL schemes. Atmos Environ 39(1):73–84

Fenner D, Meier F, Scherer D, Polze A (2014) Spatial and temporal air temperature variability in Berlin, Germany, during the years 2001–2010. Urban Clim 10:308–331

Fenner D, Meier F, Bechtel B, Otto M, Scherer D (2017) Intra and inter local climate zone variability of air temperature as observed by crowdsourced citizen weather stations in berlin, germany. Meteorol Z 26(5):525–547

Fenner D, Holtmann A, Meier F, Langer I, Scherer D (2019) Contrasting changes of urban heat island intensity during hot weather episodes. Environ Res Lett 14(12):124013

Flanner MG (2009) Integrating anthropogenic heat flux with global climate models. Geophys Res Lett 36(2)

Foken T (2016) Angewandte Meteorologie - Mikrometeorologische Methoden, vol 3. Springer Spektrum, New York

Fortuniak K, Kłysik K, Wibig J (2006) Urban–rural contrasts of meteorological parameters in Łódź. Theor Appl Climatol 84(1–3):91–101

Friedrich K, Kaspar F (2019) Rückblick auf das Jahr 2018 - das bisher wärmste Jahr in Deutschland (in German). Deutscher Wetterdienst, Tech rep

Heilman J, Brittin C, Neale C (1989) Fetch requirements for bowen ratio measurements of latent and sensible heat fluxes. Agric For Meteorol 44(3):261–273

Jänicke B, Meier F, Fenner D, Fehrenbach U, Holtmann A, Scherer D (2017) Urban-rural differences in near-surface air temperature as resolved by the central europe refined analysis (cer): sensitivity to planetary boundary layer schemes and urban canopy models. Int J Climatol 37(4):2063–2079

Karsisto P, Fortelius C, Demuzere M, Grimmond CS, Oleson KW, Kouznetsov R, Masson V, Järvi L (2016) Seasonal surface urban energy balance and wintertime stability simulated using three land-surface models in the high-latitude city Helsinki. Q J R Meteorol Soc 142(694):401–417

Kaspar F, Müller-Westermeier G, Penda E, Mächel H, Zimmermann K, Kaiser-Weiss A, Deutschländer T (2013) Monitoring of climate change in germany-data, products and services of germany's national climate data centre. Adv Sci Res 10(1):99–106

Kessler E (1969) On the distribution and continuity of water substance in atmospheric circulations. On the distribution and continuity of water substance in atmospheric circulations, vol 10. American Meteorological Society, Boston, pp 1–84

Kikegawa Y, Genchi Y, Yoshikado H, Kondo H (2003) Development of a numerical simulation system toward comprehensive assessments of urban warming countermeasures including their impacts upon the urban buildings' energy-demands. Appl Energy 76(4):449–466

Kikegawa Y, Tanaka A, Ohashi Y, Ihara T, Shigeta Y (2014) Observed and simulated sensitivities of summertime urban surface air temperatures to anthropogenic heat in downtown areas of two japanese major cities, tokyo and osaka. Theor Appl Climatol 117(1):175–193

Kottek M, Grieser J, Beck C, Rudolf B, Rubel F (2006) World Map of the Köppen-Geiger climate classification updated. Meteorol Z 15(3):259–263

Krayenhoff ES, Santiago JL, Martilli A, Christen A, Oke TR (2015) Parametrization of drag and turbulence for urban neighbourhoods with trees. Boundary-Layer Meteorol 156(2):157–189

Kuik F, Lauer A, Churkina G, Denier van der Gon HAC, Fenner D, Mar KA, Butler TM (2016) Air quality modelling in the berlin-brandenburg region using wrf-chem v3.7.1.: sensitivity to resolution of model grid and input data. Geosci Model Dev 9(12):4339–4363

Lemonsu A, Grimmond CSB, Masson V (2004) Modeling the surface energy balance of the core of an old mediterranean city: Marseille. J Appl Meteorol 43(2):312–327

Lemonsu A, Viguié V, Daniel M, Masson V (2015) Vulnerability to heat waves: Impact of urban expansion scenarios on urban heat island and heat stress in Paris (France). Urban Clim 14

Magli S, Lodi C, Lombroso L, Muscio A, Teggi S (2015) Analysis of the urban heat island effects on building energy consumption. Int J Energy Environ Eng 6(1):91–99

Martilli A, Clappier A, Rotach MW (2002) An urban surface exchange parameterisation for mesoscale models. Boundary-Layer Meteorol 104:261–304

Masson V (2000) A physically-based scheme for the urban energy budget in atmospheric models. Boundary-Layer Meteorol 94(3):357–397

Mauder M, Foken T (2011) Documentation and Instruction Manual of the Eddy-Covariance Software Package TK3. Universität Bayreuth, Bayreuth, Tech rep, Abteilung Mikrometeorologie

Meier F, Fenner D, Grassmann T, Otto M, Scherer D (2017) Crowdsourcing air temperature from citizen weather stations for urban climate research. Urban Clim 19:170–191

Mellor GL, Yamada T (1982) Development of a turbulence closure model for geophysical fluid problems. Rev Geophys 20(4):851–875

Moncrieff J, Massheder J, de Bruin H, Elbers J, Friborg T, Heusinkveld B, Kabat P, Scott S, Soegaard H, Verhoef A (1997) A system to measure surface fluxes of momentum, sensible heat, water vapour and carbon dioxide. J Hydrol 188–189:589–611

Moriwaki R, Kanda M, Senoo H, Hagishima A, Kinouchi T (2008) Anthropogenic water vapor emissions in tokyo. Water Resour Res 44(11)

Mussetti G, Brunner D, Allegrini J, Wicki A, Schubert S, Carmeliet J (2020) Simulating urban climate at sub-kilometre scale for representing the intra-urban variability of Zurich, switzerland. Int J Climatol 40(1):458–476

Napoly A, Grassmann T, Meier F, Fenner D (2018) Development and application of a statistically-based quality control for crowdsourced air temperature data. Front Earth Sci 6(2296–6463):118

Nordbo A, Järvi L, Haapanala S, Moilanen J, Vesala T (2013) Intra-city variation in urban morphology and turbulence structure in Helsinki, Finland. Boundary-Layer Meteorol 146(3):469–496

Ohashi Y, Genchi Y, Kondo H, Kikegawa Y, Yoshikado H, Hirano Y (2007) Influence of air-conditioning waste heat on air temperature in Tokyo during summer: numerical experiments using an urban canopy model coupled with a building energy model. J Appl Meteorol Climatol 46(1):66–81

Ohashi Y, Kikegawa Y, Ihara T, Sugiyama N (2014) Numerical simulations of outdoor heat stress index and heat disorder risk in the 23 wards of Tokyo. J Appl Meteorol Climatol 53(3):583–597

Oke T (1982) The energetic basis of the urban heat island. Q J R Meteorol Soc 108:1–24
Panofsky HA, Townsend AA (1964) Change of terrain roughness and the wind profile. Q J R Meteorol Soc 90(384):147–155
Paolini R, Zani A, MeshkinKiya M, Castaldo VL, Pisello AL, Antretter F, Poli T, Cotana F (2017) The hygrothermal performance of residential buildings at urban and rural sites: sensible and latent energy loads and indoor environmental conditions. Energy Build 152:792–803
Pigeon G, Moscicki MA, Voogt JA, Masson V (2008) Simulation of fall and winter surface energy balance over a dense urban area using the TEB scheme. Meteorol Atmos Phys 102(3–4):159–171
Raschendorfer M, Simmer C, Gross P (2003) Parameterisation of turbulent transport in the atmosphere. In: Neugebauer HJ, Simmer C (eds) Dynamics of multiscale earth systems, vol 97. Springer, Berlin, pp 167–185
Ritter B, Geleyn JF (1992) A comprehensive radiation scheme for numerical weather prediction models with potential applications in climate simulations. Mon Wea Rev 120(2):303–325
Rockel B, Castro CL, Pielke RA Sr, von Storch H, Leoncini G (2008a) Dynamical downscaling: assessment of model system dependent retained and added variability for two different regional climate models. J Geophys Res Atmos 113(D21)
Rockel B, Will A, Hense A (2008b) The regional climate model cosmo-clm (cclm). Meteorol Z 17(4):347–348
Roessner S, Segl K, Bochow M, Heiden U, Heldens W, Kaufmann H (2011) Potential of hyperspectral remote sensing for analyzing the urban environment, vol 4. Wiley, Hoboken, pp 49–61
Rosenberg NJ, Black BL, Verma SB (1984) Microclimate: the biological environment, 2nd editon. J Climatol 4(3):339–340
Sailor DJ (2011) A review of methods for estimating anthropogenic heat and moisture emissions in the urban environment. Int J Climatol 31(2):189–199
Salamanca F, Martilli A (2010) A new building energy model coupled with an urban canopy parameterization for urban climate simulations-part II. Validation with one dimension off-line simulations. Theor Appl Climatol 99(3–4):345–356
Salamanca F, Krpo A, Martilli A, Clappier A (2010) A new building energy model coupled with an urban canopy parameterization for urban climate simulations-part I. Formulation, verification, and sensitivity analysis of the model. Theor Appl Climatol 99(3–4):331–344
Salamanca F, Martilli A, Tewari M, Chen F (2011) A study of the urban boundary layer using different urban parameterizations and high-resolution urban canopy parameters with wrf. J Appl Meteorol Climatol 50(5):1107–1128
Salamanca F, Martilli A, Yagüe C (2012) A numerical study of the Urban Heat Island over Madrid during the DESIREX (2008) campaign with WRF and an evaluation of simple mitigation strategies. Int J Climatol 32(15):2372–2386
Salamanca F, Georgescu M, Mahalov A, Moustaoui M, Wang M, Svoma B (2013) Assessing summertime urban air conditioning consumption in a semiarid environment. Environ Res Lett 8(3)
Salamanca F, Georgescu M, Mahalov A, Moustaoui M, Wang M (2014) Anthropogenic heating of the urban environment due to air conditioning. J Geophys Res Atmos 119(10):5949–5965
Salamanca F, Georgescu M, Mahalov A, Moustaoui M (2015) Summertime response of temperature and cooling energy demand to urban expansion in a semiarid environment. J Appl Meteorol Climatol 54(8):1756–1772
Santiago JL, Martilli A (2010) A dynamic urban canopy parameterization for mesoscale models based on computational fluid dynamics reynolds-averaged navier-stokes microscale simulations. Boundary-Layer Meteorol 137(3):417–439
Schlomann B, Gruber E, Eichhammer W, Kling N, Diekmann J, Ziesing HJ, Rieke H, Wittke F, Herzog T, Barbosa M, Lutz S, Broeske U, Merten D, Falkenberg D, Nill M, Kaltschmitt M, Geiger B, Kleeberger H, Eckl R (2004) Energieverbrauch der privaten Haushalte und des Sektors Gewerbe, Handel, Dienstleistungen (GHD). Fraunhofer Institut, Tech rep
Schubert S (2013) Development and evaluation of a double-canyon urban canopy scheme, and estimation of urban heat island mitigation effects. PhD thesis, Freie Universität zu Berlin
Schubert S, Grossman-Clarke S (2013) The Influence of green areas and roof albedos on air temperatures during Extreme Heat Events in Berlin, Germany. Meteorol Z 22(2):131–143
Schubert S, Grossman-Clarke S (2014) Evaluation of the coupled COSMO-CLM/DCEP model with observations from BUBBLE. Q J R Meteorol Soc 140(685):2465–2483
Schubert S, Grossman-Clarke S, Martilli A (2012) A double-canyon radiation scheme for multi-layer urban canopy models. Boundary-Layer Meteorol 145(3):439–468
Skarbit N, Stewart ID, Unger J, Gal T (2017) Employing an urban meteorological network to monitor air temperature conditions in the "local climate zones" of szeged, hungary. Int J Climatol 37(S1):582–596

Smiatek G, Rockel B, Schättler U (2008) Time invariant data preprocessor for the climate version of the cosmo model (cosmo-clm). Meteorol Z 17(4):395–405
Stadtwerk München (2019) Gasverbrauch im Jahresverlauf (in German). Stadtwerke München, Tech rep
Statistisches Bundesamt (2018) Fachserie 3 Reihe 5.1 - Bodenfläche nach Art der tatsächlichen Nutzung (in German). Statistisches Bundesamt, Tech rep
Stewart ID, Oke TR (2012) Local climate zones for urban temperature studies. Bull Am Meteorol Soc 93(12):1879–1900
Takane Y, Kusaka H, Kondo H (2015) Investigation of a recent extreme high-temperature event in the tokyo metropolitan area using numerical simulations: the potential role of a 2hybrid" foehn wind. Q J R Meteorol Soc 141(690):1857–1869
Takane Y, Kikegawa Y, Hara M, Ihara T, Ohashi Y, Adachi SA, Kondo H, Yamaguchi K, Kaneyasu N (2017) A climatological validation of urban air temperature and electricity demand simulated by a regional climate model coupled with an urban canopy model and a building energy model in an Asian megacity. Int J Climatol 37(April):1035–1052
Tiedtke M (1989) A comprehensive mass flux scheme for cumulus parameterization in large-scale models. Mon Wea Rev 117(8):1779–1800
Trusilova K, Früh B, Brienen S, Walter A, Masson V, Pigeon G, Becker P (2013) Implementation of an urban parameterization scheme into the regional climate model COSMO-CLM. J Appl Meteorol Climatol 52(10):2296–2311
Trusilova K, Schubert S, Wouters H, Früh B, Grossman-Clarke S, Demuzere M, Becker P (2016) The urban land use in the COSMO-CLM model: A comparison of three parameterizations for Berlin. Meteorol Z 25(2):231–244
Umweltbundesamt, (2013) Gebäudeklimatisierung (in German). Umweltbundesamt, Tech rep
Vickers D, Mahrt L (1997) Quality control and flux sampling problems for tower and aircraft data. J Atmos Oceanic Technol 14(3):512–526
Walikewitz N, Jänicke B, Langner M, Meier F, Endlicher W (2015) The difference between the mean radiant temperature and the air temperature within indoor environments: A case study during summer conditions. Build Environ 84:151–161
Webb EK, Pearman GI, Leuning R (1980) Correction of flux measurements for density effects due to heat and water vapour transfer. Q J R Meteorol Soc 106(447):85–100
Wicker LJ, Skamarock WC (2002) Time-splitting methods for elastic models using forward time schemes. Mon Wea Rev 130(8):2088–2097
Wouters H, Demuzere M, Ridder KD, van Lipzig NP (2015) The impact of impervious water-storage parametrization on urban climate modelling. Urban Clim 11:24–50
Wouters H, Demuzere M, Blahak U, Fortuniak K, Maiheu B, Camps J, Tielemans D, Van Lipzig NP (2016) The efficient urban canopy dependency parametrization (SURY) v1.0 for atmospheric modelling: description and application with the COSMO-CLM model for a Belgian summer. Geosci Model Dev 9(9):3027–3054
Yagüe C, Zurita E, Martinez A (1991) Statistical analysis of the madrid urban heat island. Atmos Environ B 25(3):327–332